


ORIGINAL PAPER

Open Access



Geology along the Bedretto tunnel: kinematic and geochronological constraints on the evolution of the Gotthard Massif (Central Alps)

Markus Rast^{1*} , Andrea Galli², Jonas B. Ruh¹, Marcel Guillong² and Claudio Madonna¹

Abstract

The unlined Bedretto tunnel crosses large parts of the pre-Triassic basement of the Gotthard massif (Central Alps), giving the possibility to study late-Variscan plutonic rocks (Rotondo granite) and their Caledonian (poly-)metamorphic host rocks (Tremola and Prato series). The Rotondo granite consists mostly of an equigranular, fine-grained granite and to a lesser extent of a porphyritic granite. Commonly, the Rotondo granite is massive or only slightly foliated. Ductile deformation is localized along discrete shear zones composed of granitic or quartz-biotite-rich lithologies. This paper reviews the geology of the Bedretto tunnel with emphasis on the Rotondo granite and presents constraints based on kinematic, microstructural, and U–Pb geochronological evidence, which can be summarized as follows: (1) Both granitic and quartz-biotite-rich shear zones (QB-SZ) in the Rotondo granite generally dip moderately to steeply towards north and are related to top-to-south reverse shearing, indicating south-verging backthrusting during the exhumation of the Gotthard massif. (2) Zircons from both the equigranular and porphyritic Rotondo granite show overlapping ²⁰⁶Pb/²³⁸U-age ranges of 285–319 Ma and 280–335 Ma, respectively, which indicate that both are part of the same late-Variscan magmatic episode. Almost no older inherited cores are reported. (3) In zircons from a QB-SZ, 30% of the concordant age spots scatter between 339 and 589 Ma. This suggests that the parent material of the QB-SZ is unrelated to the magmatic episode that formed the Rotondo granite, but rather that the QB-SZ represent sheared xenoliths within the granite.

Keywords: Gotthard massif, Bedretto Underground Laboratory for Geosciences and Geoenergies, Rotondo granite, Shear zones, Strain localization, Microstructures, Geochronology, U–Pb dating with zircons

1 Introduction

The ca. 5 km-long Bedretto tunnel (or ‘Bedretto window’) was constructed from 1971 to 1982 as a southeast–northwest oriented adit to the main Furka base tunnel (Fig. 1). Since 2019, ETH Zurich has been operating the Bedretto Underground Laboratory for Geosciences and

Geoenergies (BULGG). At the BULGG, techniques for extracting geothermal energy from low permeability rocks (Engineered Geothermal Systems, EGS) are tested under conditions as close as possible to the reality of future EGS projects (Gischig et al., 2020).

The Bedretto tunnel crosses the southern Gotthard massif, which is structurally a back-folded nappe (Milnes, 1974), and therefore the term ‘Gotthard nappe’ is often applied (e.g. Berger et al., 2017). However, the term ‘Gotthard massif’ is still widely used and will also be employed in the present study. The Bedretto tunnel offers continuous outcrop conditions and crosses

Editorial handling: Stefan Schmid.

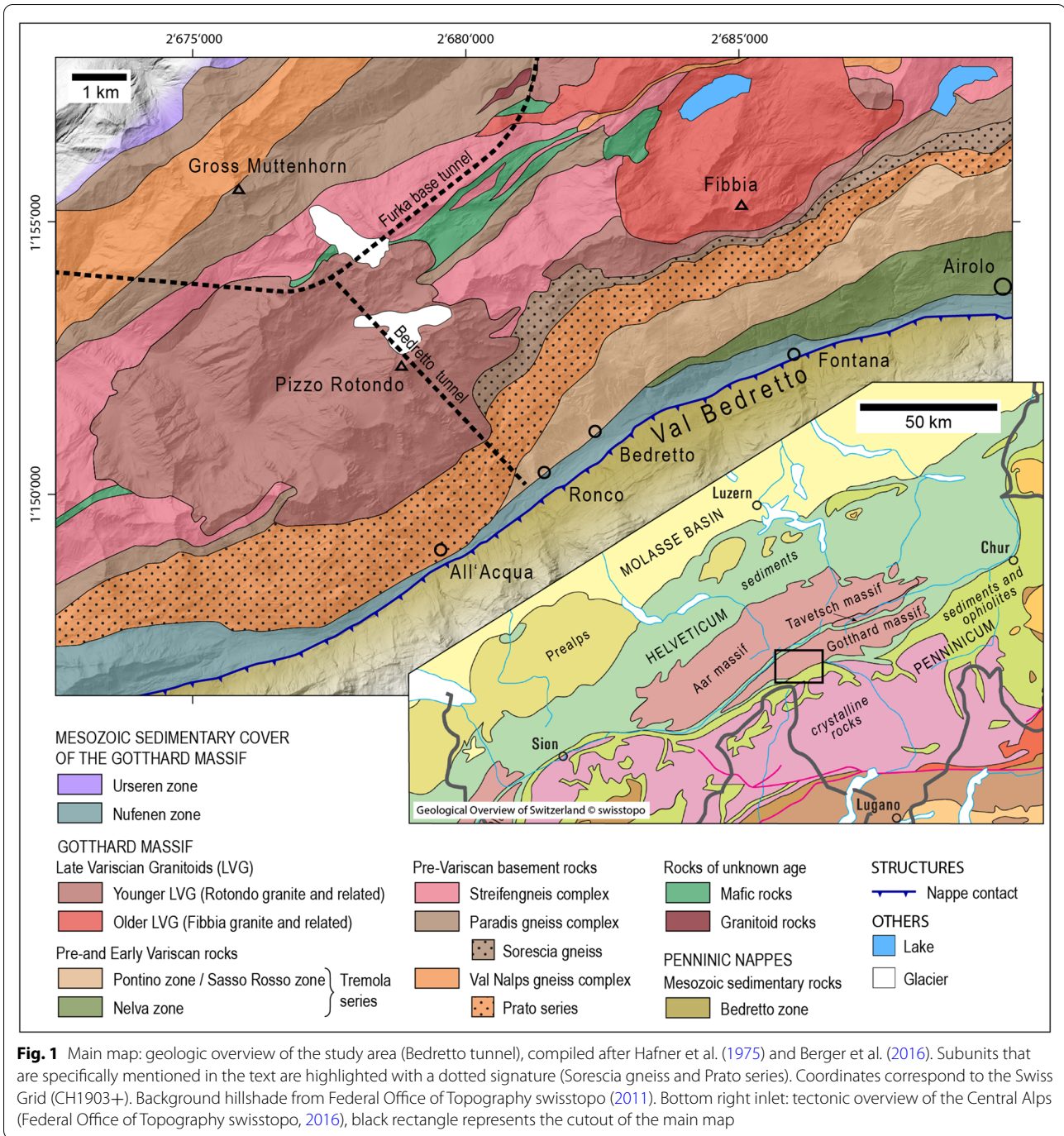
*Correspondence: markus.rast@erdw.ethz.ch

¹ Department of Earth Sciences, Geological Institute, ETH Zürich, Zurich, Switzerland

Full list of author information is available at the end of the article



© The Author(s) 2022. **Open Access** This article is licensed under a Creative Commons Attribution 4.0 International License, which permits use, sharing, adaptation, distribution and reproduction in any medium or format, as long as you give appropriate credit to the original author(s) and the source, provide a link to the Creative Commons licence, and indicate if changes were made. The images or other third party material in this article are included in the article's Creative Commons licence, unless indicated otherwise in a credit line to the material. If material is not included in the article's Creative Commons licence and your intended use is not permitted by statutory regulation or exceeds the permitted use, you will need to obtain permission directly from the copyright holder. To view a copy of this licence, visit <http://creativecommons.org/licenses/by/4.0/>.



from southeast to northwest three geological units of the Gotthard massif (Keller and Schneider, 1982): the Tremola series from tunnel meter (TM) 0 to TM 434, the Prato series (TM 434 to TM 1138), and the Rotondo granite (TM 1138 to TM 5218). Previous studies mainly focused on brittle faulting, geotechnical properties and hydrogeological characteristics of the Rotondo granite

(e.g. Lützenkirchen, 2002; Lützenkirchen and Loew, 2011; Jordan, 2019; Gischig et al., 2020).

The Rotondo granite is part of the late-Variscan granitoids (e.g. Mercolli et al., 1994; Labhart, 2005). It is mostly equigranular and fine-grained (Labhart, 2005), although a porphyritic variety with sharp contact to the equigranular granite is exposed in the central part of the tunnel (Schneider, 1985). Previous studies suggested that

the Rotondo granite is nearly undeformed (e.g. Hafner, 1958). However, in addition to an often recognizable weak foliation (Lützenkirchen and Loew, 2011), centimeter to meter thick shear zones with granitic composition and darker shear zones commonly occur. The latter were previously classified as strongly sheared lamprophyres (Schneider, 1985), although the mineralogical composition questions their interpretation as former mafic dykes. Irrespective of their origin, these rocks display a considerably stronger fabric than the host granite, indicating that their protolith was more susceptible to ductile deformation than the granite (Lützenkirchen, 2002). The identification of their parental material is crucial to understand rheological contrasts and related ductile deformation in the Rotondo granite.

Age of ductile deformation and development of a foliation in the Rotondo granite are still a matter of debate (e.g. Nunes and Steiger, 1974; Guerrot and Steiger, 1991; Labhart, 2005; Lützenkirchen and Loew, 2011). Lützenkirchen and Loew (2011) interpreted the foliation in the Rotondo granite to be of late-Variscan age, whereas Alpine deformation remained localized along discrete shear zones. In contrast, Marquer (1990) interpreted the foliation in the nearby late-Variscan Fibbia granite to be entirely of Alpine age. Labhart (2005) attributed the lack of a similarly pronounced foliation in the Rotondo granite to its lower content of phyllosilicates.

This paper reviews the regional geological setting and site characteristic of the Bedretto tunnel, with emphasis on the Rotondo granite. It also aims at providing a better reservoir characterization that may serve as basis for future studies at BULGG. Existing data are supplemented with new field and microstructural observations in order to relate kinematics and dynamic recrystallization associated with the ductile deformation of the Rotondo granite to the regional tectonic framework. Our results indicate that the relative uplift of the Gotthard massif was partly accommodated by steep, south-verging backthrusts. New geochronological U–Pb data show that both the equigranular and porphyritic varieties of the Rotondo granite formed during the same late-Variscan magmatic episode, whereas the darker shear zones are derived from xenoliths originating from paragneisses that hosted the Rotondo granite.

2 Regional geological setting

The Gotthard massif ranges about 80 km in WSW–ENE direction and about 10 km in NNW–SSE direction (Fig. 1). To the north, it is bounded by the Urseren zone, a parautochthonous sedimentary cover separating the Gotthard massif from the Aar massif. To the south, the parautochthonous sedimentary cover of the Nufenen zone separates the Gotthard massif from the Mesozoic

sediments of the Penninic units (e.g. Mercolli et al., 1994; Labhart, 2005; Berger et al., 2017).

2.1 Geological units

The units of the Gotthard massif crossed by the Bedretto tunnel will be described from older to younger below (Sect. 2.1.1 to 2.1.3). The following additional units occur in the vicinity of the Bedretto tunnel: a few hundred meters wide zone of amphibolites, the Streifengneiss complex, and the Sorescia gneiss, the latter being counted as part of the Paradis gneiss complex (Fig. 1). The Streifengneiss complex is composed of Silurian orthogneisses, of which the most prominent is characterized by a distinct linear texture (Huber, 1943; Nunes and Steiger, 1974; Sergeev and Steiger, 1993; Labhart, 2005; Berger et al., 2017). The Sorescia gneiss consists of migmatitic two-mica gneisses (Hafner, 1958; Steiger, 1962; Keller et al., 1987; Labhart, 2005; Berger et al., 2017), which are very similar to some rocks of the adjacent Prato series, and a clear distinction is often not obvious (Hafner, 1958).

2.1.1 Prato series (Val Nalps gneiss complex)

The part of the pre-Variscan Val Nalps gneiss complex (Berger et al., 2017) crossed by the Bedretto tunnel is often referred to as ‘Prato series’ (e.g. Steiger, 1962; Hafner et al., 1975; Labhart, 2005). This is a ca. 20 km long and up to ca. 2 km wide, elongated zone striking parallel to the Gotthard massif (Fig. 1) and consisting of two-mica-alkali-feldspar \pm garnet gneisses and schists, hornblende gneisses and schists, and amphibolites (Hafner, 1958; Steiger, 1962; Keller et al., 1987). The mineralogical assemblages of the different rock types of the Prato series is summarized by Labhart (2005) after Hafner (1958) and Keller et al. (1987). Banded hornblende schists and amphibolites dominate the northern and southern part, whereas the central part consists mainly of two-mica gneisses and schists with lenses of amphibolites, hornblende schists, and biotite schists (Hafner, 1958). The Prato series has a complicated internal structure characterized by steep isoclinal folds. Moreover, the alternation of different rock types and migmatization led to narrow banding on the centimeter to tens of meters scale (Labhart, 2005). The rocks are strongly foliated and display a steeply north- or south-plunging mineral lineation defined by mica grains (Steiger, 1962).

2.1.2 Tremola series

The pre- and early Variscan Tremola series is a ca. 20 km long and ca. 2 km wide zone, which separates the Prato series in the northwest from the parautochthonous sedimentary cover of the Nufenen zone in the southeast (Fig. 1). Berger et al. (2017) used the term ‘Tremola Gneiss Complex’, while in this study the earlier term

‘Tremola series’ is used. Based on the relative occurrence of different rock types, Steiger (1962) subdivided the Tremola series into Pontino zone, Sasso Rosso zone, and Nelva zone. The Tremola series is a sequence of metasedimentary rocks consisting mainly of mica-rich gneisses, mica-schists, hornblende-schists, hornblende-gneisses, and minor calc-silicate rocks, amphibolites, and quartzites (Steiger, 1962; Keller et al., 1987). The mineralogical assemblages of the different rock types of the Tremola series are summarized by Labhart (2005) after Hafner (1958), Keller et al. (1987) and Steiger (1962). Usually, the mineral assemblage and structure are highly variable. Changes between different rock types often occur within meters (Steiger, 1962; Labhart, 2005).

2.1.3 Rotondo and Fibbia granites

The main part of the Late to post-Variscan Rotondo granite is located in the central part of the Gotthard massif, extending about 8 km in WSW–ENE direction and about 5 km in NNW–SSE direction (Fig. 1). In addition, four smaller granite bodies further to the northeast are classified as Rotondo granite, although they are not connected in map view (Labhart, 2005). The Rotondo granite consists to a large extent of an equigranular, fine-grained granite, while in certain domains it also consists of a more biotite-rich and porphyroclastic granite, such as in the central part of the Bedretto tunnel (Schneider, 1985). Locally, steeply dipping aplite dykes and lamprophyre dykes cross-cut the Rotondo granite (Hafner, 1958; Oberhänsli, 1986; Labhart, 2005).

The nearby Fibbia granite is located northeast of the Rotondo granite and extends about 5 km in WSW–ENE direction and about 3 km in NNW–SSE direction (Fig. 1). The Fibbia granite is porphyritic with up to 2–3 cm large, idiomorphic alkali feldspar grains. Due to a well-developed foliation, the Fibbia granite is also described as ‘granite-gneiss’ in the literature (Labhart, 2005). A comparison between the composition of the Fibbia and Rotondo granites based on literature data is shown in Table 1.

U–Pb single grain ID-TIMS zircon dating on zircons extracted from feldspars (Sergeev et al., 1995) showed a slightly younger age for the equigranular Rotondo granite (294 ± 1.1 Ma) than for the Fibbia granite

(299.4 ± 1.2 Ma). No age determinations for the porphyritic Rotondo granite exist so far.

In the Rotondo granite, a weakly developed main foliation dips steeply towards NW (Lützenkirchen and Loew, 2011). Ductile deformation appears to be localized within steeply northward-dipping granitic shear zones, or darker shear zones interpreted as former lamprophyres (Schneider, 1985; Lützenkirchen and Loew, 2011). In contrast, the Fibbia granite displays a steeply dipping, WSW–ENE striking penetrative foliation and a steeply dipping mineral lineation defined by biotite, sericite, and feldspar plunging sub-parallel to the foliation dip direction (Hafner, 1958; Marquer, 1990). Centimeter-to meter-thick shear zones strike sub-parallel to the regional foliation (Marquer, 1990), as is the case in the Rotondo granite.

2.2 Tectonic evolution and metamorphism

2.2.1 Pre-Alpine tectonics and metamorphism

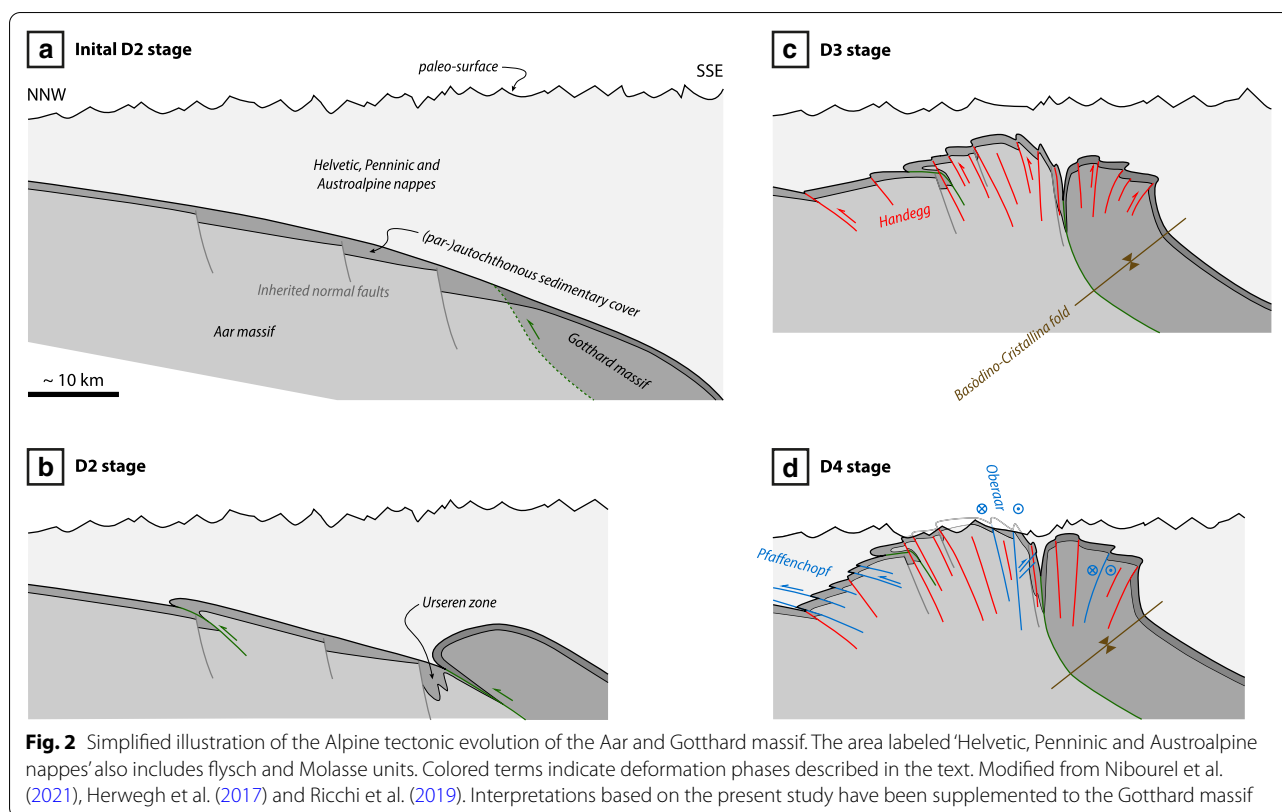
Paragneisses of different basement units of the European continental crust contain detrital zircons with ages between 0.6 and 3.4 Ga, which are interpreted as originating from source rocks of a pan-African orogen (Schaltegger and Gebauer, 1999). In mafic rocks that intruded into paragneisses of the Val Nalps gneiss complex, Biino (1994) recognized an eclogitic mineral assemblage partially replaced by a granulite facies assemblage. This was interpreted as the result of subduction (eclogite facies) followed by nearly isothermal uplift (granulite facies), whereby the migmatization of the host paragneisses was related to granulite facies conditions. According to Biino (1994) and Schaltegger (1994), the age of eclogite facies metamorphism is provided by the Caledonian U–Pb zircon intercept age of 467–475 Ma determined by Oberli et al. (1994), who has dated zircons without inherited cores from metagabbros.

In the field, cross-cutting relationships suggest that migmatization of the paragneisses pre-dated the intrusion of the Streifengneis (Meccolli et al., 1994), which according to zircon ages occurred around 439 Ma (Sergeev and Steiger, 1993). Subsequently, Variscan folds (Schlingen tectonics) affected both, Streifengneis and already existing paragneisses (e.g. Prato series, Sorescia gneiss) (Meccolli et al., 1994). A study of Variscan structures by Pettke and Klaper (1992) revealed a medium to

Table 1 Composition of the Rotondo and Fibbia granites based on Hafner (1958), Labhart (2005) and Steck (1976)

	Qz (%)	Kfs (%)	Pl (%)	Bt (%)	Ph (%)	Accessories
Rotondo granite	25–35	20–40	10–25	3–8	Accessory	Grt, Ph, Chl, Ep, Ap, opaques, Zrn, Fl
Fibbia granite	20–30	25–40	20–30	ca. 10	5–10	Chl, Ep, Grt, Zrn, Ap

Mineral abbreviations according to Whitney and Evans (2010)



steeply inclined foliation dipping towards the NNW, a relatively flat alkali feldspar lineation plunging towards the ENE, and late isoclinal folds with relatively flat axes plunging towards the east. A pre-Alpine quartz-feldspar matrix in the Sorescia gneiss contains sericitized andesine, which indicates Variscan amphibolite facies metamorphism (Nunes and Steiger, 1974).

The Tremola series was interpreted by Mercolli et al. (1994) as representing metasediments, accreted in the Middle Paleozoic (Devonian) to the then existing part of the European continental crust (to which the Gotthard massif is counted today). This interpretation is based on the lack of high-grade pre-Devonian metamorphism and the intrusion of late-Variscan granitoids (Gamsboden granite) into the Tremola series.

2.2.2 Alpine tectonics and metamorphism

The Alpine tectonic evolution of the Central Alps has been intensely studied (e.g. Marquer, 1990; Grujic and Mancktelow, 1996; Schmid et al., 1997; Pfiffner et al., 2002; Maxelon and Mancktelow, 2005; Herwegh et al., 2017; Steck et al., 2019; Nibourel et al., 2021) and is summarized in the following, with emphasis on the Gotthard massif:

1. The detachment of the Penninic nappes (with the Gotthard massif as their structurally lowest part) between late Eocene to Oligocene was accompanied by the detachment of the Ultrahelvetic and Helvetic sedimentary cover from the Gotthard, Tavetsch, and southern Aar massif at around ~ 40 Ma (Schmid et al., 1997), but in any case before the thrusting of the Gotthard massif onto the Aar massif started (e.g. Pfiffner, 2010; Herwegh et al., 2017). Structures of this first deformation phase ('D1 stage') are generally rarely preserved (Labhart, 2005), and the basement of the Gotthard massif was not affected by this phase (Berger et al., 2017).
2. A second phase of deformation ('D2 stage') is associated with the thrusting of the Gotthard massif together with its parautochthonous sedimentary cover onto the southern Aar massif (e.g. Berger et al., 2017; Herwegh et al., 2017; Ricchi et al., 2019, Figs. 2a and b). Due to a lack of a metamorphic temperature jump at the boundary between Gotthard and Aar massif, Herwegh et al. (2017) concluded that the Gotthard massif was thrusting onto the Aar massif prior to the Alpine thermal peak, which occurred at ~ 19 – 18 Ma in this area (Wiederkehr et al., 2009; Berger et al., 2017; Ricchi et al., 2019). A NE–SW striking foliation with a steep lineation in the Got-

thard massif is commonly thought to be related to this deformation stage (e.g. Schmid et al., 1997; Labhart, 2005).

3. Development of large-scale synforms in the Penninic zone ('D3 stage') resulted in the formation of the 'northern steep belt' (Milnes, 1974): from east to west, these synforms are known as the Chiéra fold, which evolved around 14–13 Ma (Ricchi et al., 2019), the Basòdino-Cristallina fold (Grujic and Mancktelow, 1996), and the Berisal fold, which evolved between 15 and 9 Ma (Pfiffner et al., 2002). It is generally assumed that the formation of the 'northern steep belt' also led to the steepening of the Gotthard massif and a corresponding large-scale back-folding of the southern Gotthard massif (e.g. Maxelon and Mancktelow, 2005; Herwegh et al., 2017; Ricchi et al., 2019), while the 'D3 stage' in the Aar massif is related to steep reverse faults ('Handegg phase', e.g. Berger et al., 2017; Herwegh et al., 2017, Fig. 2c). Both the steepening of the Gotthard massif and the steep reverse faults in the Aar massif are the result of the delamination of the lower crust and the subsequent buoyancy driven uplift (Herwegh et al., 2017). The 'D3' steepening of the Gotthard massif led to an almost vertical to overturned foliation in the southern Gotthard massif (Tremola series) and its parautochthonous sedimentary cover (Nufenen zone) (Labhart, 2005), and resulted in the present steep orientation of the Permo-Carboniferous sediments of the Urseren zone (Wyss, 1986). Marquer (1990) related steep backthrusts in the Gotthard massif to the large-scale synforms in the Penninic zone. A model of minor steepening of the Gotthard massif indicated by a dome-like geometry of the Rotondo granite body (Kissling et al., 1978; Labhart, 2005) was refuted by kinematic analyses (e.g. Schmid et al., 1997; Wiederkehr et al., 2009).
4. The end of the European slab rollback during the middle to late Miocene resulted in northwest-directed sub-horizontal reverse faulting at the northern front of the Aar massif ('Pfaffenchoopf' phase, after ~12 Ma) and dextral strike-slip within the Aar massif ('Oberaar' phase, ~11.5–7 Ma) (Herwegh et al., 2017; Ricchi et al., 2019, Fig. 2d). Dextral strike-slip faults in the Gotthard massif are further discussed in Sect. 5.2.2 with respect to the Rotondo granite. 'Oberaar' and 'Pfaffenchoopf' phases are summarized by some authors as the 'D4 stage', which is further associated with back-thrusting in the southern Aar massif (Herwegh et al., 2017; Nibourel et al., 2021, Fig. 2d).

Across the Gotthard massif, the Alpine metamorphic grade generally increases from upper greenschist facies in the northwest to greenschist-amphibolite facies transition in the southeast (Bousquet et al., 2012). Steck (1976) demonstrated that the mineral assemblage of the Rotondo granite was recrystallized to a large extent during the Alpine orogeny under greenschist facies conditions.

3 Geology along the Bedretto tunnel

The geological characterization of the Bedretto tunnel is based on both existing data (tunnel section of Schneider, 1985, a geometric unfolding in top fan, SW-wall, base and NE-wall) and new data acquired during the present study. All position data in this paper correspond to the distance along the tunnel axis from its entrance, the so-called tunnel meter (TM). Petrology, microstructures, and kinematics of 30 representative samples were studied (sample location and type of analyses are shown in Table 2). Structural features and rock types along the Bedretto tunnel are displayed in the simplified cross-section of Fig. 3a, which includes data from Keller and Schneider (1982), Schneider (1985), and data of this study. A detailed petrological description of the Bedretto tunnel in high spatial resolution is given in the tunnel section of Schneider (1985). The orientation of foliation, fault zones (> 10 cm wide), and shear zones were plotted against the distance along the tunnel axis (Fig. 3b) and in lower-hemisphere equal-area projections (Fig. 4). The orientation data of the foliation and fault zones are mainly adopted from the existing tunnel section of Schneider (1985), while the data of the shear zones are from the present study.

3.1 Tremola and Prato series

Rocks of the Tremola series occur between the southern entrance of the tunnel and TM 434 (Fig. 3a). They typically consist of centimetric to decametric alternations of schists and gneisses composed of varying amounts of quartz, plagioclase, biotite, white mica, chlorite, garnet, and epidote, ± garnet-bearing hornblende-schists, amphibolites, and subordinate calcsilicates, which produces a characteristic compositional banding sub-parallel to the main foliation. Between TM 0 and TM 355, the rocks of the Tremola series are affected by toppling (Keller and Schneider, 1982; Masset and Loew, 2010, Fig. 3a). This gravitationally driven slope failure caused a Quaternary re-orientation of the main structures and resulted in a main foliation dipping moderately towards the NW (Fig. 3). After TM 355, the main foliation dips steeply towards the SE (Figs. 3b and 4a).

Rocks of the Prato series occur between TM 434 and TM 1138. The contact between the Tremola and

Table 2 Collected hand samples from the Rotondo granite used for thin section investigation by optical microscopy

TM	Wall	Sample name	Description	ZI
1156	NE	B19-1156	Equigranular granite	
1258	NE	B20-1258	Equigranular granite	
1350	NE	B19-1350	Granitic shear zone	
1417	NE	B19-1417	Equigranular granite	×
1755	NE	B20-1755	Equigranular granite	
2253	SW	B20-2253	Equigranular granite	
2742	SW	B20-2742	Equigranular granite	
2801	NE	B20-2801	Quartz-biotite-rich shear zone	×
2801	SW	B20-2801-2	Quartz-biotite-rich shear zone	
3145	SW	B20-3145	Porphyritic granite	
3147	SW	B20-3147	Quartz-biotite-rich shear zone	
3147	SW	B20-3147-1	Quartz-biotite-rich shear zone	
3147	NE	B20-3147-2	Quartz-biotite-rich shear zone	
3155	NE	B20-3155	Enclave in granite	
3247	SW	B20-3247	Porphyritic granite	×
3320	NE	B20-3320	Aplitic dyke	
3375	NE	B20-3375	Enclave in granite	
3380	NE	B20-3380	Enclave in granite	
3385	NE	B20-3385	Porphyritic granite	
3615	NE	B20-3615	Enclave in granite	
3751	NE	B20-3751	Equigranular granite	
4173	NE	B20-4173-2	Quartz-biotite-rich shear zone	
4173	SW	B20-4173-1	Quartz-biotite-rich shear zone	
4182	SW	B20-4182	Enclave in granite	
4191	SW	B20-4191	Aplitic dyke	
4253	SW	B20-4253	Equigranular granite	
4367	SW	B20-4367	Enclave in granite	
4384	NE	B20-4384	Enclave in granite	
4759	NE	B20-4759	Equigranular granite	
5158	SW	B20-5158	Equigranular granite	

Samples used for zircon investigations are marked with '×' in the corresponding column (ZI). The uncertainty in the TM-measurements is about ±1 m

Prato series is sharp (Fig. 5a). From TM 434 to TM 635, the Prato series consists typically of amphibolites with bands of biotite-rich gneisses and leucocratic quartzo-feldspatic gneisses. From TM 635 to TM 1138, hornblende bearing rocks are less common and the Prato series is dominated by alternating centimeters- to several meters-thick, foliation-parallel bands of leucocratic two-mica-gneisses, and melanocratic (\pm garnet-bearing) biotite-gneisses, interpreted as leucosomes and melanosomes in migmatites. The main foliation in the Prato series is defined by the preferred orientation of mica and generally dips steeply towards the SE, as in the Tremola series (Figs. 3b and 4a). However, from approximately TM 1000 onward, the foliation becomes progressively steeper and dips to NW

towards the contact with the Rotondo granite (Fig. 3b). Shear sense indicators are often not well established and contradictory shear senses occur. However, the general trend shows an upward movement of the northern block (Fig. 5b), which is particularly apparent at the SE- and NW-contact of the Prato series (Figs. 5a and c, respectively).

3.2 Rotondo granite

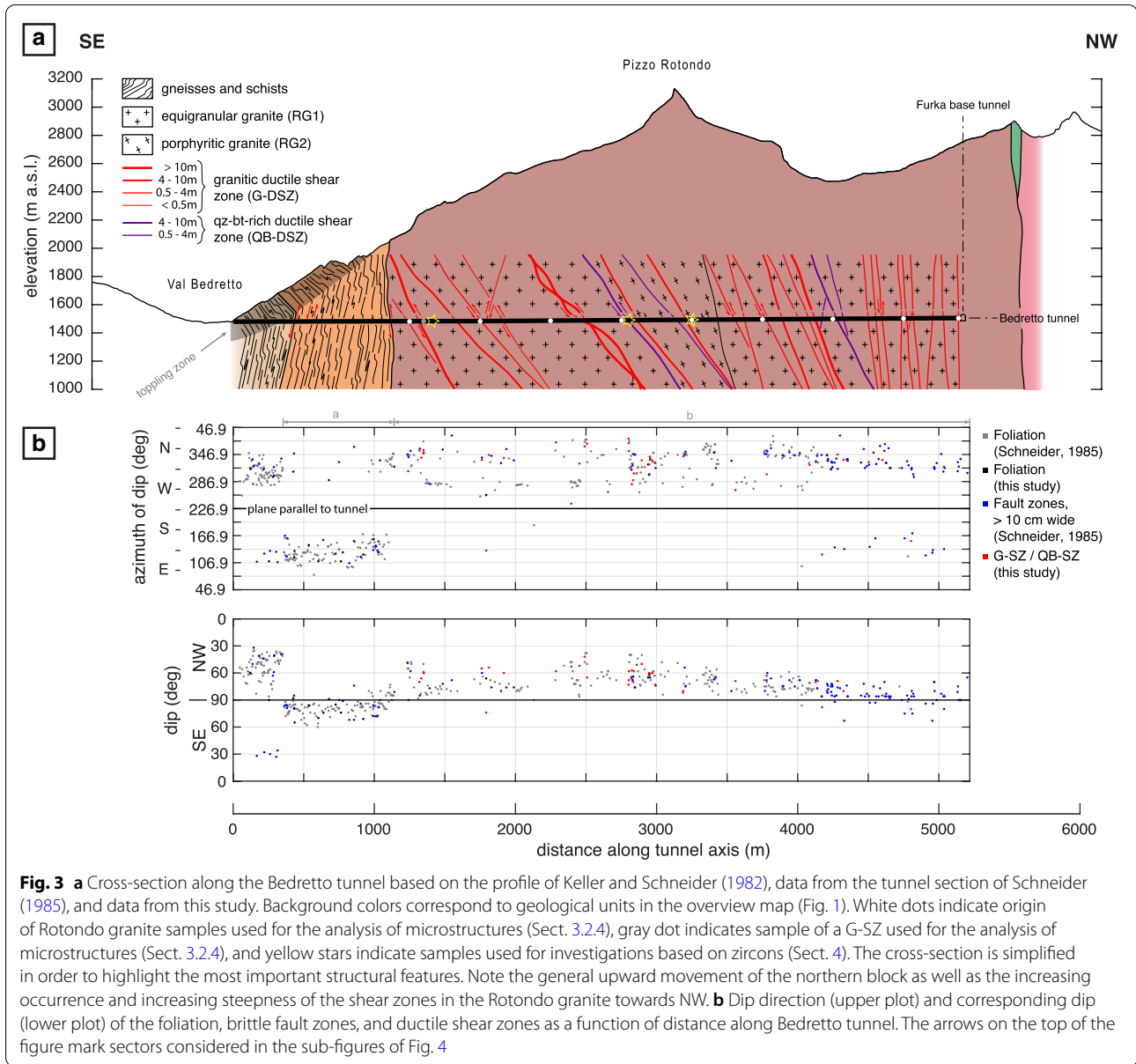
3.2.1 Equigranular (RG1) and porphyritic (RG2) granite varieties

The Rotondo granite occurs from TM 1138 to TM 5218 (the NW tunnel end). The contact to the Prato series is sharp and characterized by top-to-south shearing (Fig. 5c). The Rotondo granite is highly deformed away from the contact up to TM 1143. The main body of the Rotondo granite can be subdivided into an equigranular variety (referred to as RG1) and a porphyritic variety (referred to as RG2), the latter occurring only between TM 2805 and TM 3437 on the NE wall and between TM 2807 and TM 3431 on the SW wall. The two varieties of granite are separated in the SE by a quartz-biotite-rich shear zone (Sect. 3.2.3). In the NW, RG2 and RG1 are separated by a sharp contact (Fig. 5d).

The main phases of RG1 are quartz, alkali feldspar, plagioclase, and biotite, which display an equigranular to inequigranular, interlobate texture (Figs. 6a and 7a–e). Three types of quartz with different grain size ranges and different grain boundary shapes occur (Sect. 3.2.4). Alkali feldspar forms anhedral grains in the mm range (Fig. 7b). Plagioclase commonly forms anhedral grains in the mm range, and lamellar twinning is widespread (Figs. 7b and c). Biotite crystals form ca. 1 mm large sub- to anhedral grains, commonly partly replaced by chlorite. In some samples, the biotite content is very low, while muscovite, which occurs usually as accessory mineral, is more abundant (Figs. 7b, c, and e). Further accessory minerals are epidote, apatite, zircon, titanite, opaques, and garnet. The garnet crystals are often subhedral in shape and are found within alkali feldspar grains.

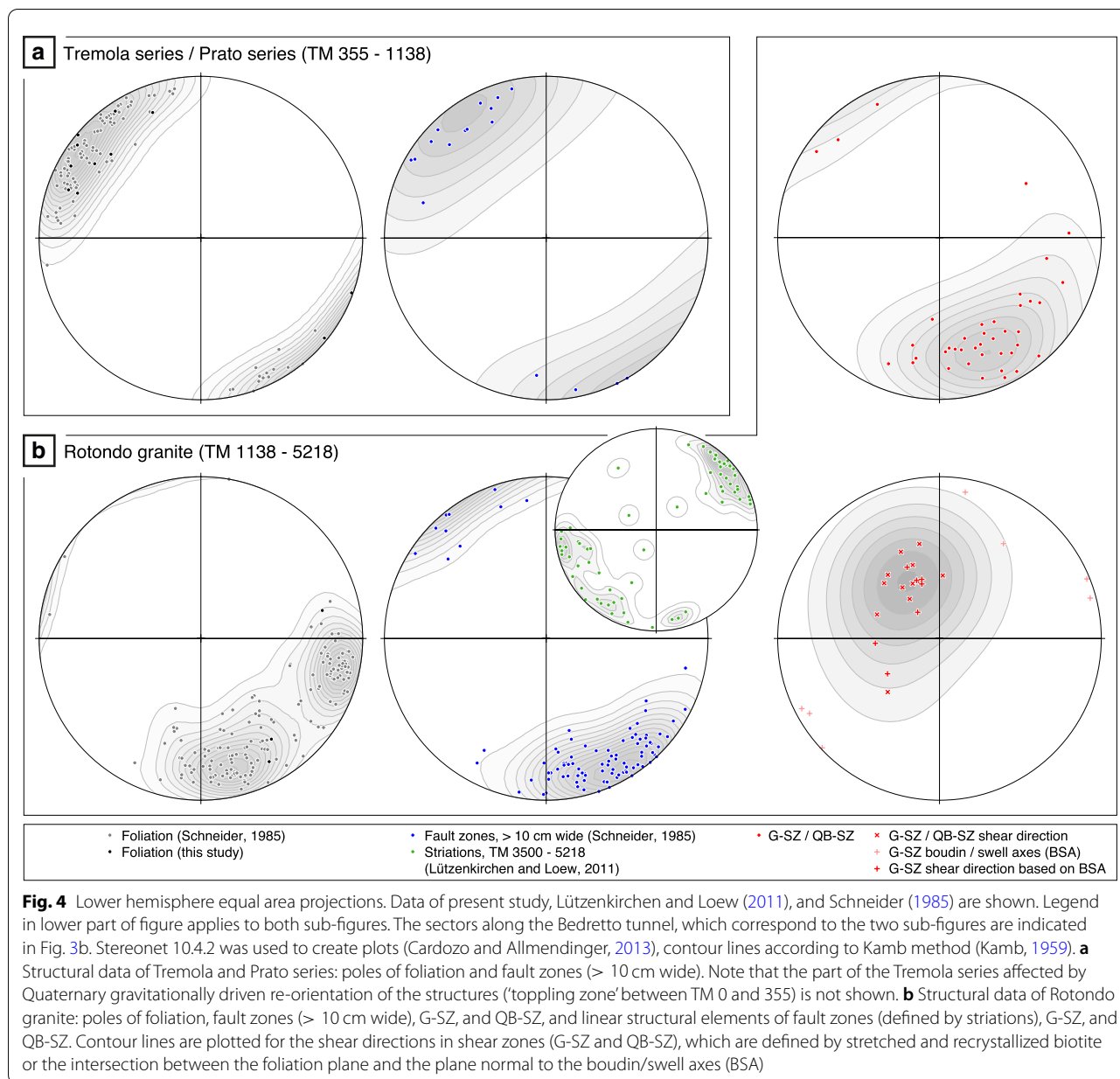
In terms of mineralogical composition, the RG2 variety does not differ from RG1, but the proportion of the different phases varies. RG2 is coarser grained, displays a distinct inequigranular texture with interlobate grain boundaries, has a higher biotite content than RG1, and has up to ca. 3 cm large, subhedral to anhedral alkali feldspar porphyroclasts with perthite unmixing (Figs. 6b and 7f). Grain sizes and shapes of the other minerals in samples of RG2 are roughly equivalent to those from RG1.

A main foliation defined by biotite is usually well-developed in RG2. Towards the NW contact, RG2 is more intensely foliated and appears darker than further to the southeast (Fig. 5d). In contrast, a foliation in RG1



is rather weakly developed and in some cases hardly recognizable in the field, in particular between TM 1138 and TM 2800. In this section of the tunnel, the foliation in RG1 is defined by discrete mm scale zones of biotite accumulation (possibly due to pressure solution of other minerals), which often appear to localize brittle fractures at a later stage. The stereonet in Fig. 4b indicates a bimodal distribution of foliation orientation, where two sets of foliations can be distinguished: one dipping steeply towards W, and one steeply towards N (see also Fig. 3b). However, both sets of foliations have the same overall characteristics described above.

Aplitic dykes crosscut both RG1 and RG2. According to the tunnel section of Schneider (1985), the thickness of the aplitic dykes ranges along the Bedretto tunnel from tens of centimeters to a few meters. In some of the aplitic dykes, in addition to a compositional layering, a foliation defined by fine-grained biotite is recognizable (Fig. 8). The foliation within the dykes is oriented parallel to the foliation in the adjacent granite, which indicates that the development of the foliation is younger than the intrusion of the dyke.



3.2.2 Enclaves in the Rotondo granite

Enclaves in the Rotondo granite are relatively rare from TM 1138 (contact to Prato series) up to approximately TM 2800 but more abundant from there to the NW terminus of the tunnel (TM 5218). Few meters NW of the RG2-RG1 contact, at TM 3431, an enclave in RG1 shows a larger biotite content than the surrounding RG1, alkali feldspar porphyroclasts up to about 1.5 cm, and appears to be similar to the nearby RG2 (Fig. 9a). The contact between enclave and surrounding RG1 appears diffuse and 'frayed', which indicates magma mingling.

However, enclaves with a sharp contact to the surrounding granite are also widespread between TM 2800 and TM 5218 (Fig. 9b). These enclaves are melanocratic, very fine-grained, and consist mainly of quartz, plagioclase, and biotite, with minor muscovite, epidote, calcite, and garnet (Fig. 9c). The texture is equigranular and polygonal (in particular quartz aggregates) to interlobate. Quartz forms anhedral crystals up to 0.3 mm in size with undulose extinction. Aggregates of quartz show in some cases triple junctions with angles of ~ 120° but have often irregular grain boundaries. Plagioclase grains are anhedral and up to 0.5 mm in size.



Fig. 5 Field photographs. Italic numbers correspond to tunnel meter (TM) where the images were taken. This is also valid for subsequent figures with field photographs or photomicrographs and will no longer be mentioned. **a** Contact between Tremola series in the SE and Prato series in the NW, hammer for scale. **b** Folded and sigmoidal quartz aggregates indicating top-to-south shear sense (upward movement of the northern block) in the Prato series, pencil for scale. **c** Contact between Prato series in the SE and Rotondo granite in the NW. The Rotondo granite consists at the contact to the Prato series of an approximately 5 m wide zone of highly deformed granite. Pencil for scale. **d** Contact between the porphyritic variety of the Rotondo granite (RG2) in the SE and the equigranular variety of the Rotondo granite (RG1) in the NW. Note that the RG2 is relatively strongly sheared at the contact and that the RG2 further to the SE is not as dark as in this photograph. Hammer for scale

The lamellar twinning in the plagioclase appears to be disturbed and often blurs towards the grain boundary. Biotite is subhedral with a grain size up to 0.4 mm and appears to define a weak foliation. Of the accessory minerals, epidote and muscovite are relatively widespread, while minor amounts of calcite and garnet are present.

3.2.3 Shear zones in the Rotondo granite

Lützenkirchen (2002) and Lützenkirchen and Loew (2011) focused on brittle faults in the Bedretto tunnel between TM 3500 and TM 5218 and their relationship to hydrogeological properties. They found that

brittle faulting is preferentially localized along pre-existing ductile shear zones and that these steeply NW-dipping (approximately tunnel perpendicular striking) faults mainly exhibit dextral strike-slip movement. Additional mapping of brittle faults between TM 1140 and TM 2800, supplemented by data from borehole logging, surface mapping, and aerial image mapping also revealed steeply NW-dipping discontinuities, as well as three further sets of brittle fractures: a steeply dipping E–W striking set, a steeply dipping N–S striking set and a steeply dipping tunnel parallel (NW–SE striking) set (Jordan, 2019; Gischig et al., 2020). The steeply NW-dipping faults (Lützenkirchen, 2002; Lützenkirchen and Loew, 2011;

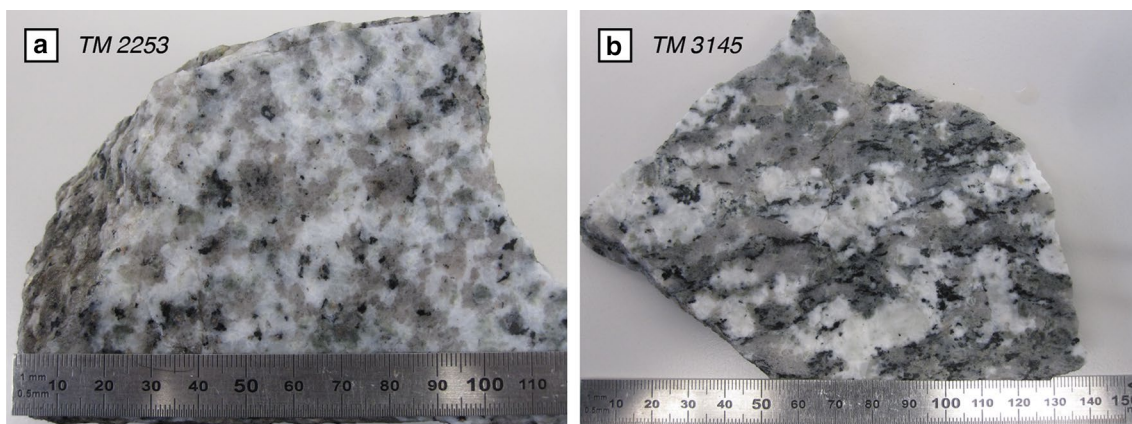


Fig. 6 Photographs of cut and wetted hand specimens taken from the Rotondo granite with macroscopically recognizable quartz (light reddish gray), plagioclase (light greenish), alkali feldspar (white), and biotite (black). **a** Equigranular variety (RG1). **b** Porphyritic variety (RG2)

Gischig et al., 2020; Jordan, 2019) fit the fault zones in the Rotondo granite (> 10 cm wide) mapped by Schneider (1985) (Fig. 4b).

In the following, we focus on ductile shear zones in the Rotondo granite along the Bedretto tunnel, since less attention has been paid to them in previous studies. In general, it can be observed that ductile strain localizes in regions with rheological contacts. This becomes apparent at the contact between the Prato series and the Rotondo granite (Fig. 5c), as well as at the contact between the two varieties of Rotondo granite (Fig. 5d). However, strain localization along rheological contacts was also observed within the same type of granite, where slight differences in grain size and composition occur (Fig. 10a). Based on the mineralogical content, the observed ductile shear zones in the Rotondo granite can be subdivided into (1) shear zones with similar mineralogy to the granite (referred to as granitic shear zones, G-SZ), and (2) shear zones containing more quartz and biotite and less feldspar relative to the G-SZ (referred to as quartz-biotite-rich shear zones, QB-SZ).

G-SZ occur in the entire Rotondo granite with thicknesses ranging from a few centimeters to more than 10 m. An increasing frequency of G-SZ can be observed from SE to NW (Fig. 3a). Between TM 1138 and TM ~2800, G-SZ are often below 0.5 m in thickness, apart from a few larger shear zones (> 4 m wide). These shear zones consist of very fine-grained rocks with a well-developed foliation defined by biotite. This gives the shear zone a slightly darker appearance compared to the relatively undeformed granite, but they are not as dark as the QB-SZ (Fig. 10a). Shear zones with thicknesses in the meter range are more common from TM ~2800 to the NW terminus (TM 5218) of the Bedretto tunnel (Figs. 10b and c). In such shear zones, feldspar clasts are

generally apparent, which gives the shear zone a ‘gneiss-like’ appearance. Figures 10d–g show thin section cutouts of a sample taken from a G-SZ (TM 1350). The sample has an inequigranular and interlobate texture, consists of the main phases quartz, alkali feldspar, plagioclase, and biotite, and contains additionally muscovite, chlorite, epidote, calcite, zircon, and opaques as accessory minerals. Apart from the calcite contained and the increased occurrence of epidote, the mineralogy essentially corresponds to RG1 samples, in particular to the sample from TM 1755 (Figs. 7b–e). Two types of quartz with different grain size ranges and different grain boundary shapes occur (Sect. 3.2.4). Alkali feldspars are up to a few millimeters in size, form anhedral grains, and show perthite unmixing. Plagioclase crystals have a grain size of up to about 1 mm, anhedral shapes, and show lamellar twinning. Biotite grains are around 0.5 mm in size, subhedral, and form a well-developed foliation.

QB-SZ are less common than G-SZ and occur between TM 2800 and the NW terminus (TM 5218) of the tunnel (Fig. 3a). The thickness ranges from the dm to the meter scale. The widest QB-SZ occurs between TM 2800 and TM 2805 (Figs. 11a–c). QB-SZ consist of dark, fine-grained rocks with a well-developed foliation defined by biotite. Besides biotite, quartz is macroscopically recognizable in this fine-grained domain. Additionally, sigmoidal quartz veins containing rigid calcite clasts in the cm range occur in the QB-SZ between TM 2800 and TM 2805 (Figs. 11b and c). Figures 11d–f show thin section cutouts of samples taken from two QB-SZ (one located between TM 2800 and TM 2805 and one at TM 3147). The QB-SZ consist of quartz, biotite and, compared to the G-SZ, a minor amount of plagioclase. In addition, the phases epidote, zircon, and in some samples calcite or muscovite are present. Quartz crystals are anhedral,

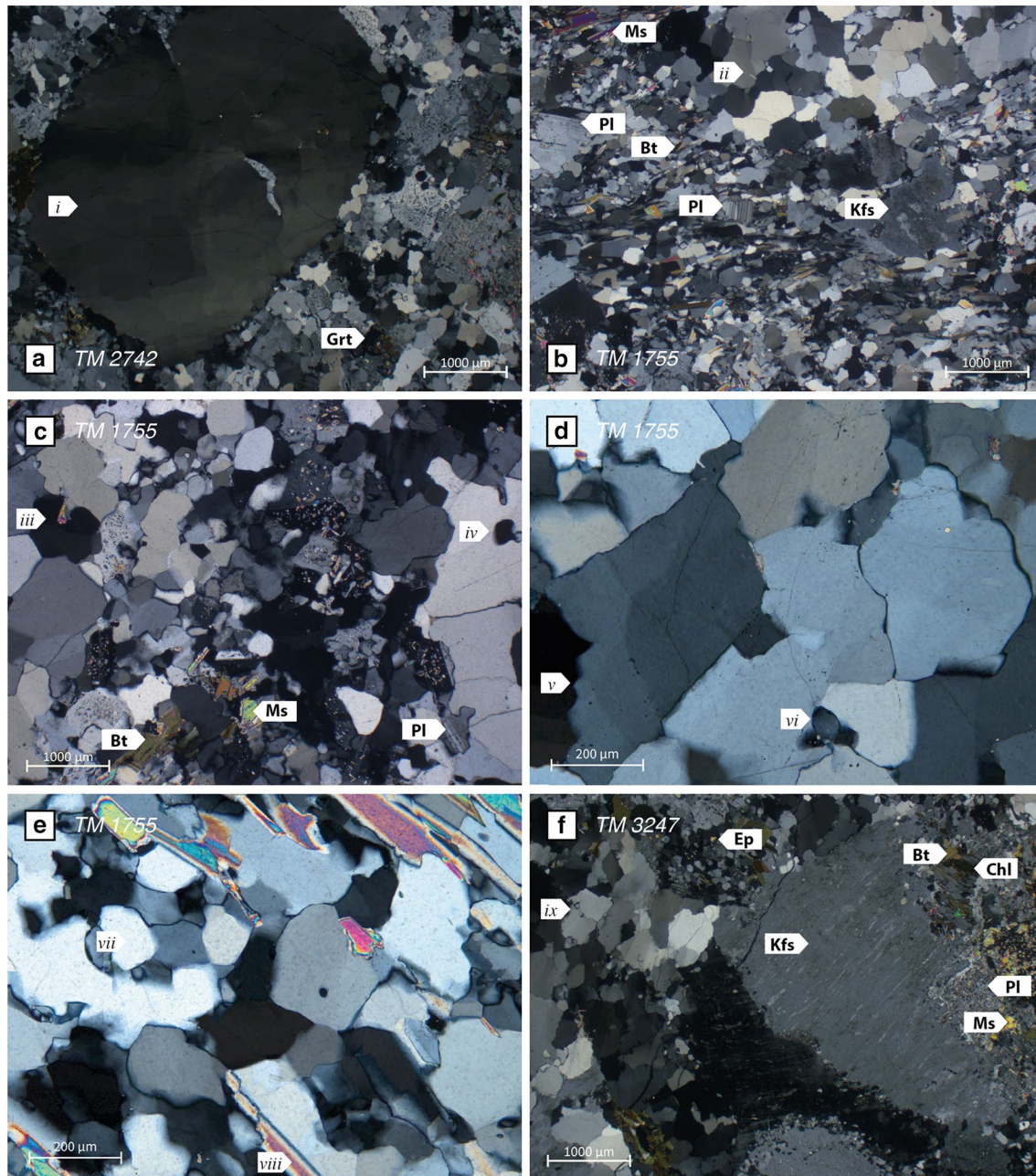


Fig. 7 Thin section cutouts of RG1 (a–e) and RG2 (f), crossed polarized light in all photomicrographs. Mineral abbreviations according to Whitney and Evans (2010) (this is also valid for subsequent figures with photomicrographs and will no longer be mentioned). The italic roman numbers correspond to descriptions related to dynamic recrystallization (Sect. 3.2.4): (i) magmatic quartz with grain size > 4 mm showing undulose extinction, (ii) dynamically recrystallized quartz in coarse-grained domain, (iii) pinning structure in coarse-grained domain, (iv) 'left-over' grain in coarse-grained domain, (v) irregular grain-boundary in coarse-grained domain, (vi) 'left-over' grain in coarse-grained domain, (vii) slightly elongated grain in fine-grained domain, (viii) potential pinning of quartz by the indicated white mica grain, (ix) coarse-grained domain in a RG2 sample

often slightly elongated parallel to biotite, and up to 0.3 mm in size (but usually below 0.1 mm). Biotites are subhedral with grains up to 0.5 mm in size and form the foliation. This is generally more pronounced in the sample from the QB-SZ at TM 3147 (Fig. 11f) than in the

QB-SZ between TM 2800 and TM 2805 (Figs. 11d and e). Plagioclase occurs as anhedral grains, which are up to 0.5 mm in size. Calcite in the sample of the wide QB-SZ (TM 2800–2805) forms relatively large (up to 0.5 mm) subhedral crystals with lamellar twins, which are

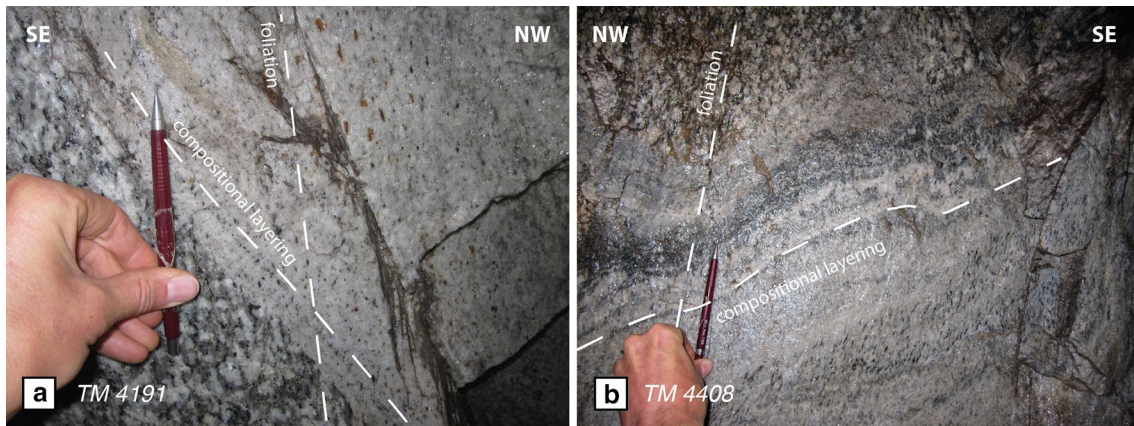


Fig. 8 Foliation in the Rotondo granite and its continuation into aplitic dykes with compositional layering at TM 4191 (a) and TM 4408 (b). Pencil for scale

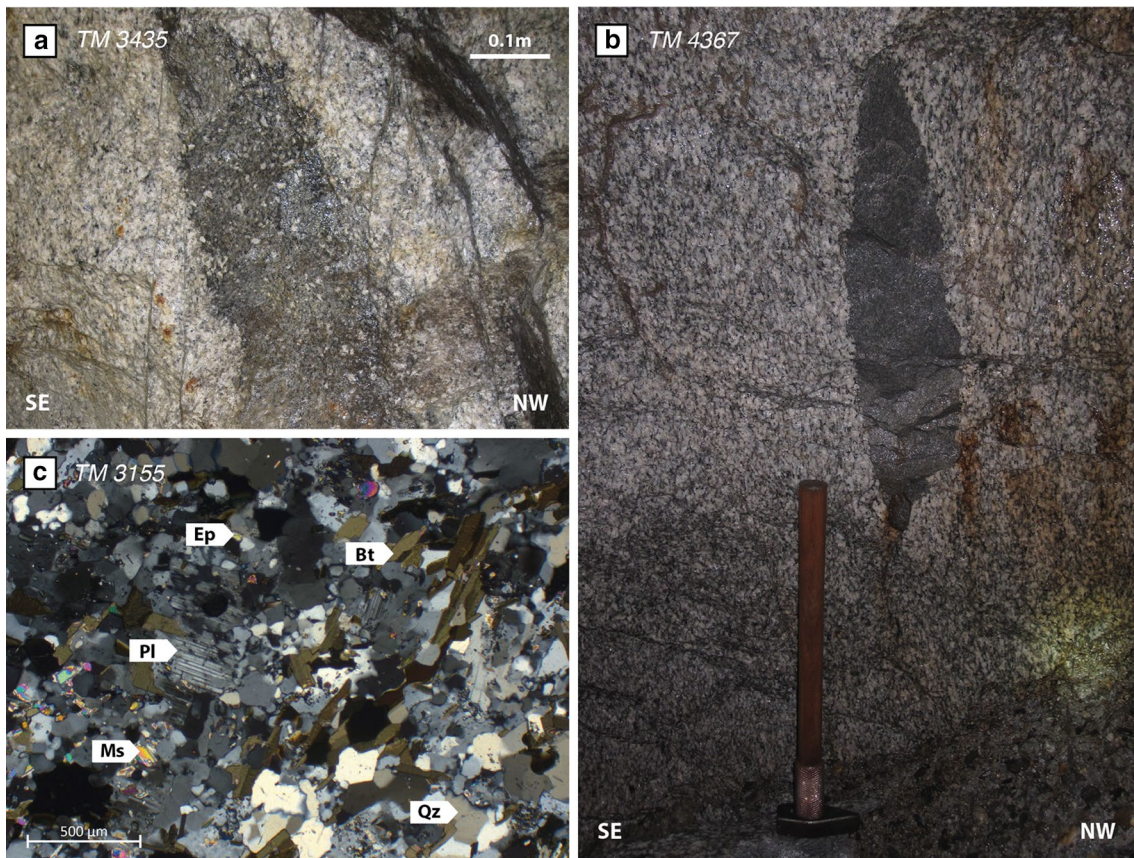


Fig. 9 a Enclave within the Rotondo granite (RG1) showing indications of magma mingling and therefore interpreted as a magmatic enclave. b Enclave in the Rotondo granite with sharp contact interpreted as xenolith, hammer for scale. c Thin section cutout of an enclave with sharp contact to the granite, which is interpreted as a xenolith (crossed polarized light)

relatively straight and about 20 μm wide. Calcite is much more abundant in the wide QB-SZ (TM 2800–2805) than in the one at TM 3147. Epidote is relatively widespread

in samples of both QB-SZ. Muscovite is present in the QB-SZ at TM 3147, in which it is parallel to biotite and has similar shapes and grain sizes as biotite.

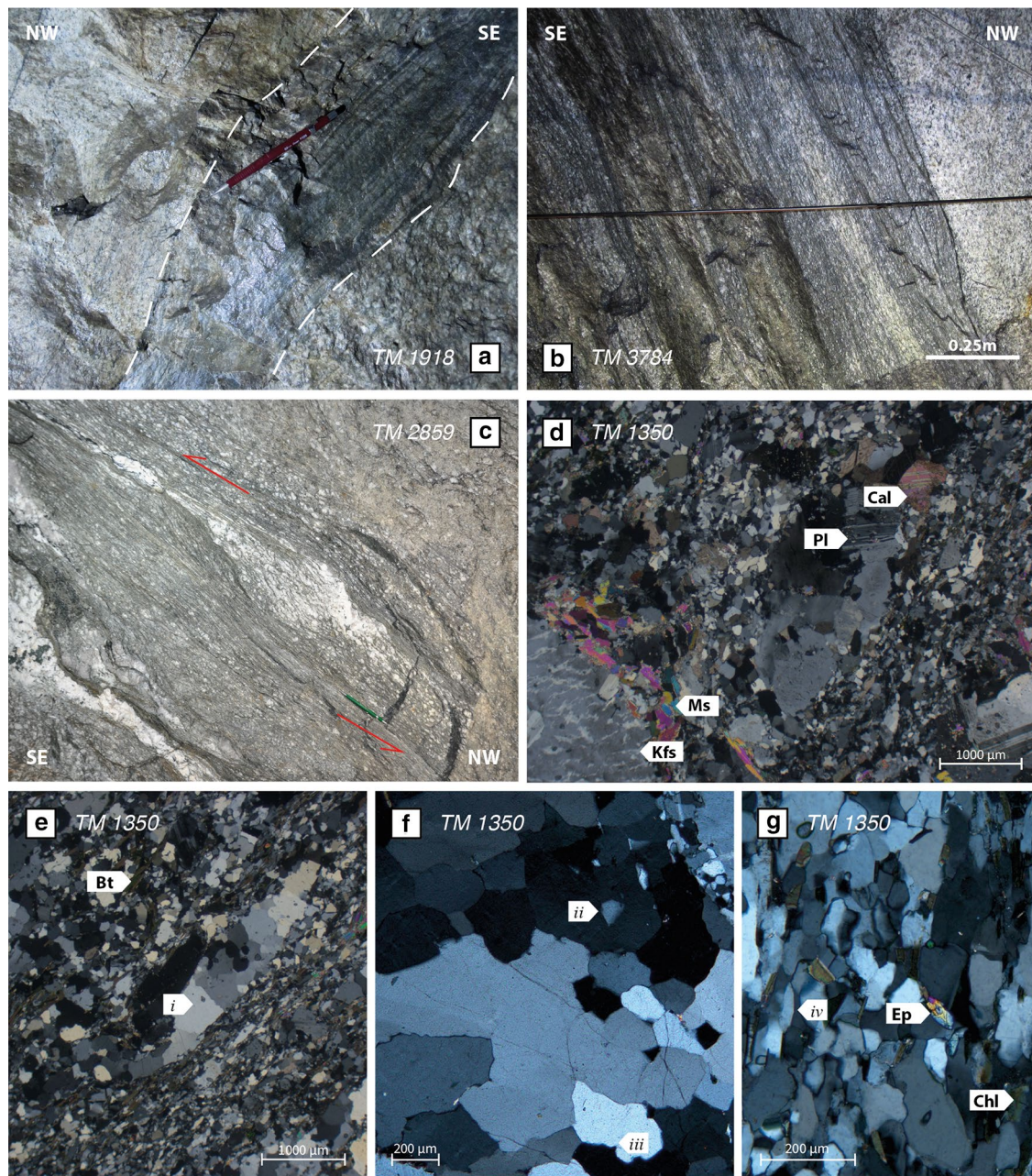


Fig. 10 Field photographs and photomicrographs of G-SZ. **a** Strain localization at the boundary between coarser grained granite in the SE and finer grained granite in the NW, pencil for scale. **b** G-SZ in the meter range, as typically observed between TM 2800 and the NW terminus of the tunnel (TM 5218). **c** Shear sense indication by sigmoidal aggregate, pencil for scale. **d–g** Thin section cutouts of a G-SZ at TM 1350. The italic roman numbers correspond to descriptions related to dynamic recrystallization (Sect. 3.2.4): (i) quartz in coarse-grained domain surrounded by fine-grained bands, (ii) 'island' grain in coarse-grained domain, (iii) irregular grain boundary in coarse-grained domain, (iv) elongated quartz grain in fine-grained domain

Both types of shear zones, G-SZ and QB-SZ, are similarly oriented and generally dip moderately to steeply towards N (Fig. 4b). The steepness of the shear zones observed in the Rotondo granite increases from SE to NW (Fig. 3). The lineation defined by stretched and

recrystallized biotite generally dip steeply towards N, and thus indicates dip-slip (Fig. 4b). Additionally, boudin and swell axes of feldspar augen, and the intersection lines of planes normal to these axes with the corresponding foliation planes, are shown in Fig. 4b.

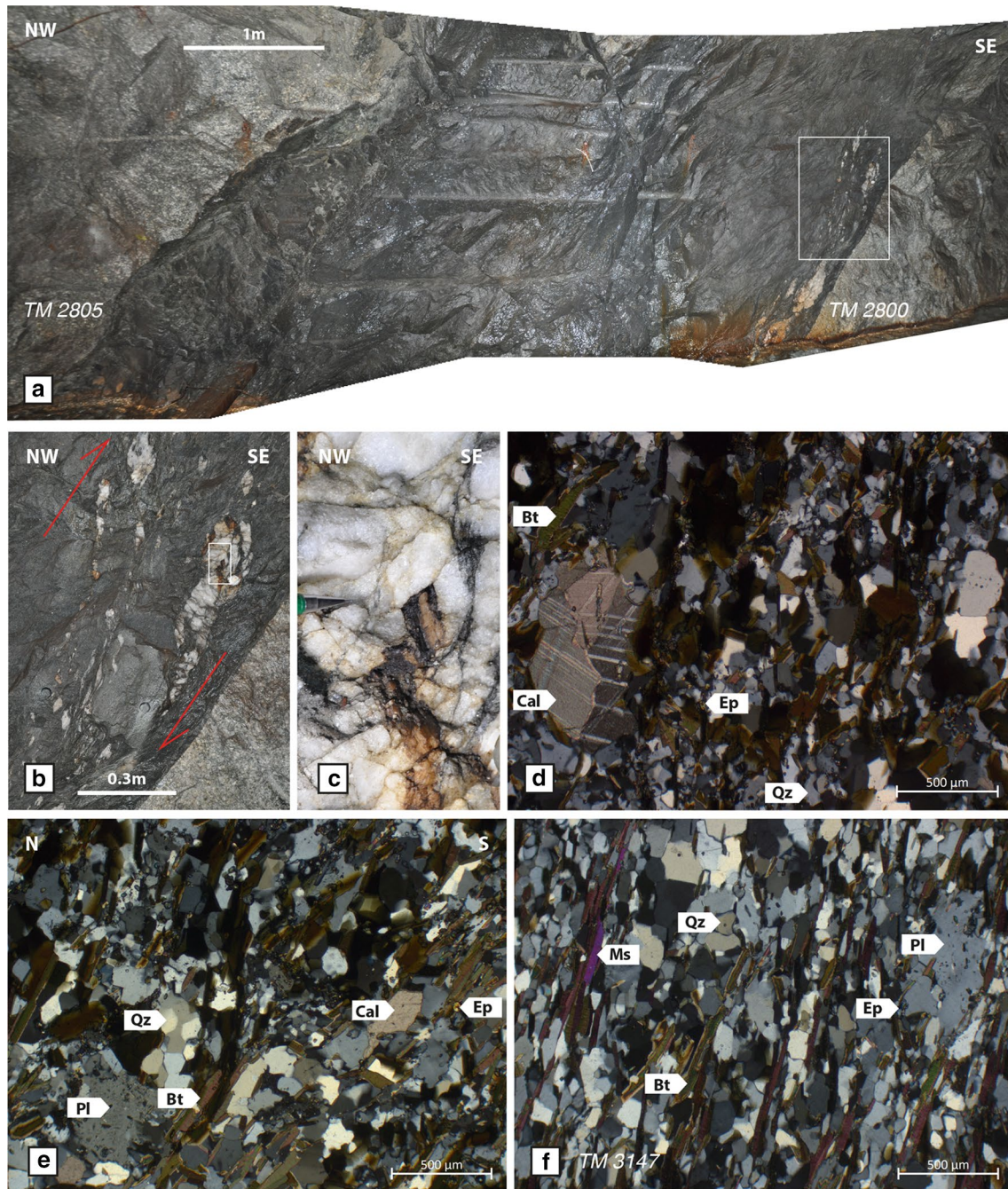


Fig. 11 Field photographs and photomicrographs of the QB-SZ between TM 2800 and TM 2805 (**a-e**) and at TM 3147 (**f**). **a** White frame indicates the close-up shown in (**b**). **b** Close-up of the SE-contact. Shear sense is indicated by sigmoidal quartz veins. White frame indicates a further close-up shown in (**c**). **c** Rigid calcite crystals (brown) inside deformed quartz (white), pencil tip for scale. **d, e** Photomicrographs of the QB-SZ between TM 2800 and TM 2805, crossed polarized light. **f** Photomicrograph of a QB-SZ at TM 3147, crossed polarized light

The latter indicate the shear direction and correspond well with the biotite lineations. The sense of shear commonly indicates upward movement of the northern block (top-to-south), for both G-SZ and QB-SZ (Figs. 10c and 11b). This upward movement of the

northern block is consistent with the sense of shear observed at the contact between Prato series and Tremola series (Fig. 5a), with the general shear sense in the Prato series (Fig. 5b), and with the shear sense observed at the contact between Prato series and Rotondo

granite (Fig. 5c). Taking into account the shear direction defined by the lineations, the shear zones in the Rotondo granite show a reverse movement with almost no strike-slip component.

3.2.4 Dynamic recrystallization in the Rotondo granite

The estimation of the mean grain sizes of dynamically recrystallized quartz in an RG1, RG2, and G-SZ sample are presented in Additional file 1, and the results are described below. Determination of grain sizes and identification of quartz was based on optical microscopy of thin sections (i.e., the data represent two-dimensional grain size distributions). Grain sizes of 80 to 121 grains per sample were measured. For samples in which quartz occurs in both fine-grained and coarse-grained domains (see below), the measurements were divided approximately equally between the two domains (i.e. 60 or 61 grains per domain). For a single grain size measurement, the mean value of the long and short axis was determined.

The samples of relatively undeformed granite show three types of quartz microstructures exhibiting different grain sizes and different grain boundary shapes: (1) In a few samples, magmatic (non-recrystallized) quartz is preserved, which occurs as anhedral grains in the mm range and shows undulose extinction (Fig. 7a). (2) Dynamically recrystallized quartz occurs within coarse-grained domains with irregular, interlobate grain boundaries (Fig. 7b to d). The grain size of quartz in these domains yielded mean values of $280 \pm 140 \mu\text{m}$ (RG1 sample from TM 1755) and $460 \pm 220 \mu\text{m}$ (RG2 sample from TM 3247). (3) Recrystallized quartz also occurs in fine-grained domains with polygonal to interlobate grain boundaries and occasionally slightly elongated grains, which, together with mica, define a foliation (Figs. 7b and e). The grain size of quartz in these domains (RG1 sample from TM 1755) is estimated as $160 \pm 80 \mu\text{m}$ (Additional file 1). Magmatic quartz is restricted to samples taken between the SE contact of the Rotondo granite (TM 1138) and TM 3500, and the relative proportion of coarse-grained recrystallized quartz tends to increase towards NW (Table 3).

No magmatic quartz is preserved in a G-SZ sample from TM 1350, but both types of recrystallized quartz described above for the relatively undeformed granite also occur in coarse-grained and fine-grained domains (Figs. 10e–g). Quartz in coarse-grained patches is surrounded by fine-grained bands (Fig. 10e), which can be also observed in relatively undeformed granite samples. An estimation of the quartz grain sizes resulted in $360 \pm 180 \mu\text{m}$ for quartz in coarse-grained domains and

Table 3 Estimation of abundance of magmatic quartz, recrystallized quartz in coarse-grained domains, and recrystallized quartz in fine-grained domains for relatively undeformed Rotondo granite samples (sample location in tunnel meter, TM)

TM	Magmatic	Coarse-grained	Fine-grained
1258	x	xxx	—
1755	—	x	xxx
2253	x	xxx	—
2742	x	—	xxx
3247	xx	xx	—
3751	—	xxx	x
4253	—	xxx	—
4759	—	xxx	—
5158	—	xxx	—

xxx = dominantly present, xx = abundantly present, x = slightly present, — = not present

$60 \pm 30 \mu\text{m}$ for quartz in fine-grained domains (Additional file 1).

4 Geochronological data

In order to corroborate the intrusion age of the Rotondo granite and to compare the two varieties observed in the Bedretto tunnel, zircons of the equigranular granite RG1 (sample B19-1417) and of the porphyritic granite RG2 (sample B20-3247) were investigated. In addition, zircons of a QB-SZ (sample B20-2801) were examined to obtain indications of the parent material of the deformed rocks and to retrieve a first-order estimation for the timing of deformation.

4.1 Methods

Samples were cut into pieces of about 10–20 cm³ and crushed by high-voltage pulse fragmentation using a SELFRAG apparatus. The resulting sand was then manually sieved into a fraction < 500 μm and a fraction > 500 μm . A Holman and Wilfley table was used to separate different density fractions from the sand with smaller grain size (< 500 μm). Zircons were identified by a stereo microscope. 75 zircons from sample B19-1417, 96 zircons from sample B20-3247, and 55 zircons from sample B20-2801 were hand-picked. Zircons were mounted on two epoxy holders and visualized by Cathodoluminescence (CL) imaging using a Jeol JSM-6390 LA scanning electron microscope (SEM) equipped with a LaB₆-filament and a Centaurus CL detector.

The isotopic composition of the zircons was measured by Laser Ablation-Inductively Coupled Plasma-Mass Spectrometry (LA-ICP-MS), using a Resonetics

Resolution Excimer argon fluoride laser ablation system equipped with a Laurin Technics Resolution S-155 ablation cell and coupled to a Thermo Element XR sector field ICP-MS. The laser ablation system was operated with the parameters shown in Additional file 2. If the internal structure of a zircon CL-image suggested domains of potentially different ages (i.g. core and rim), both domains were measured. However, this was limited by the spot size (19 μm) and therefore only possible if the zircons, respectively texturally different domains, were large enough (Additional file 3).

GJ-1 zircon standard (Jackson et al., 2004) was used as a primary reference material to correct the U–Th–Pb data for mass bias, down hole fractionation, instrumental offset, and instrumental drift. A quality control of the resulting ages was carried out by using secondary reference materials shown in Additional file 2 (Wiedenbeck et al., 1995; Sláma et al., 2008; Kennedy et al., 2014; Von Quadt et al., 2016). In order to determine the trace element composition of the zircons, the NIST-610 glass standard (Norman et al., 1996) was used for calibration (external standard) and silicon (Si) was used as an internal standard. Trace elements were measured on the same spots that were used for the age determination.

Data reduction and presentation follows the guidelines of Horstwood et al. (2016). The LA-ICP-MS data were processed using the software Iolite 4 (Paton et al., 2011). To identify discordant ages, the U–Pb data were plotted in a Wetherills concordia diagram (Wetherill, 1956). For the calculation and visualization of the U–Pb ages, the software IsoplotR was used (Vermeesch, 2018). The total uncertainty S_{tot} of the mean ages was calculated assuming a systematic error S_{sys} of 1.2% (Horstwood et al., 2016). Data that were not taken into account for the age determination and/or trace element composition analysis are indicated in Additional file 4, including the rationale for discarding the corresponding data points. A table including the results of the LA-ICP-MS measurements is presented in Additional file 4. CL-images of zircons, with indicated LA-ICP-MS spots, are shown in Additional file 3.

4.2 Results

4.2.1 Equigranular granite (RG1)

A total of 71 zircons from sample B19-1417 were analysed by CL-imaging. A total of 75 spots were measured by LA-ICP-MS. Of these, 21 measurements were performed in domains with oscillatory zoning (Figs. 12a and b), 13 in domains with slightly blurred oscillatory zoning, eleven in or close to domains with a ‘spongy texture’ (Fig. 12c), 18 in domains with strongly blurred zoning (lower zircon in Fig. 12d), and eight in domains with almost no zoning except a ‘ghost texture’ (upper zircon in Fig. 12d). The

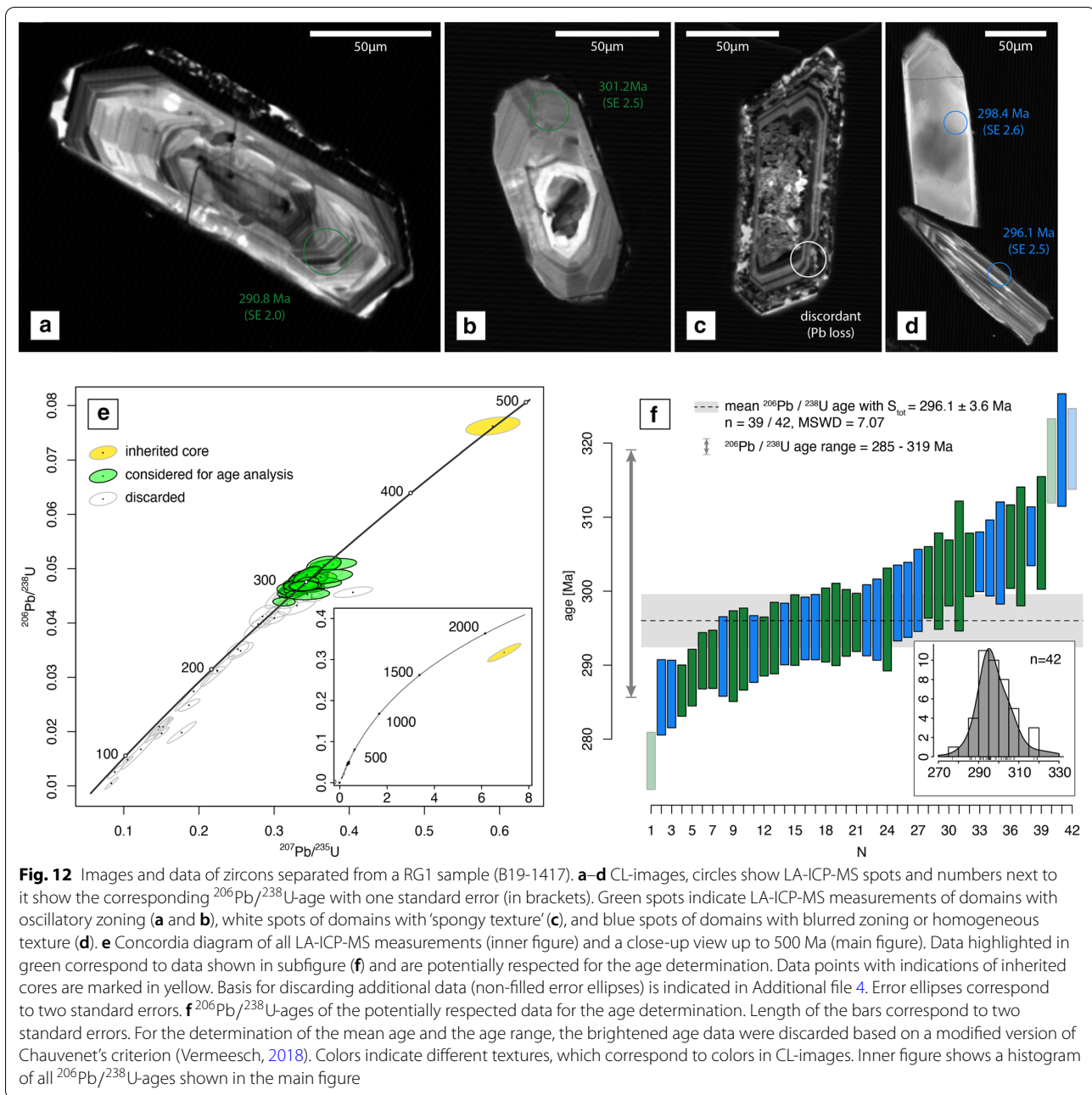
observed ‘ghost texture’ is commonly interpreted as a relict of a primary texture within recrystallized domains and the ‘spongy texture’ as a complex alteration pattern (Corfu et al. 2003). The latter is supported by the fact that affected zircons often exhibit discordance or have been discarded for the age determination due to indications of considerable Pb loss.

A total of 31 data points were discarded due to discordance or other indications on considerable Pb loss (see Additional file 4), and two data points suggest an inherited core, leaving a total of 42 data points considered for the age determination (Figs. 12e and f). For the determination of the mean age, another three outliers were rejected based on a modified version of Chauvenet’s criterion (Vermeesch, 2018) (brightened bars in Fig. 12f). The considered $^{206}\text{Pb}/^{238}\text{U}$ -ages have a range of 285–319 Ma with a distinct peak at ~ 295 Ma and a mean of 296.1 ± 3.6 Ma (Fig. 12f). However, the mean is related to a mean squared weighted deviation (MSWD) value of 7.07. The MSWD indicates the goodness of fit, where values > 1 represent either a scatter in the age distribution, which cannot be attributed to measurement uncertainties, or underestimation of the uncertainties (Horstwood et al., 2016). The latter attribution is rather unlikely, since the MSWD values of the secondary reference materials are around one (ranging from 0.52 to 1.96). Therefore it appears that the presented mean age does not correspond to a precise geological event (see also discussion in Sect. 5.3). No correlation is observed between the textures and the ages considered for the mean age and the age range (Fig. 12f).

The chondrite-normalized rare earth element (REE) composition shows a relatively steeply rising slope from La to Lu (Fig. 13a). The slope is steeper for the light rare-earth elements (LREE) than for the heavy rare-earth elements (HREE) with an average $\text{Sm}_{\text{norm}}/\text{La}_{\text{norm}}$ of 330 ± 230 (Fig. 14a). In addition, the zircons have a pronounced positive Ce anomaly with an average of 37 ± 30 and a negative Eu anomaly of 0.13 ± 0.06 (Fig. 14b). The Th–U-ratios and Zr–Hf-ratios show average values of 0.55 ± 0.25 and 51 ± 7 , respectively (Fig. 14c). No relation between trace element composition and zircon texture occurs (Figs. 13a and 14).

4.2.2 Porphyritic granite (RG2)

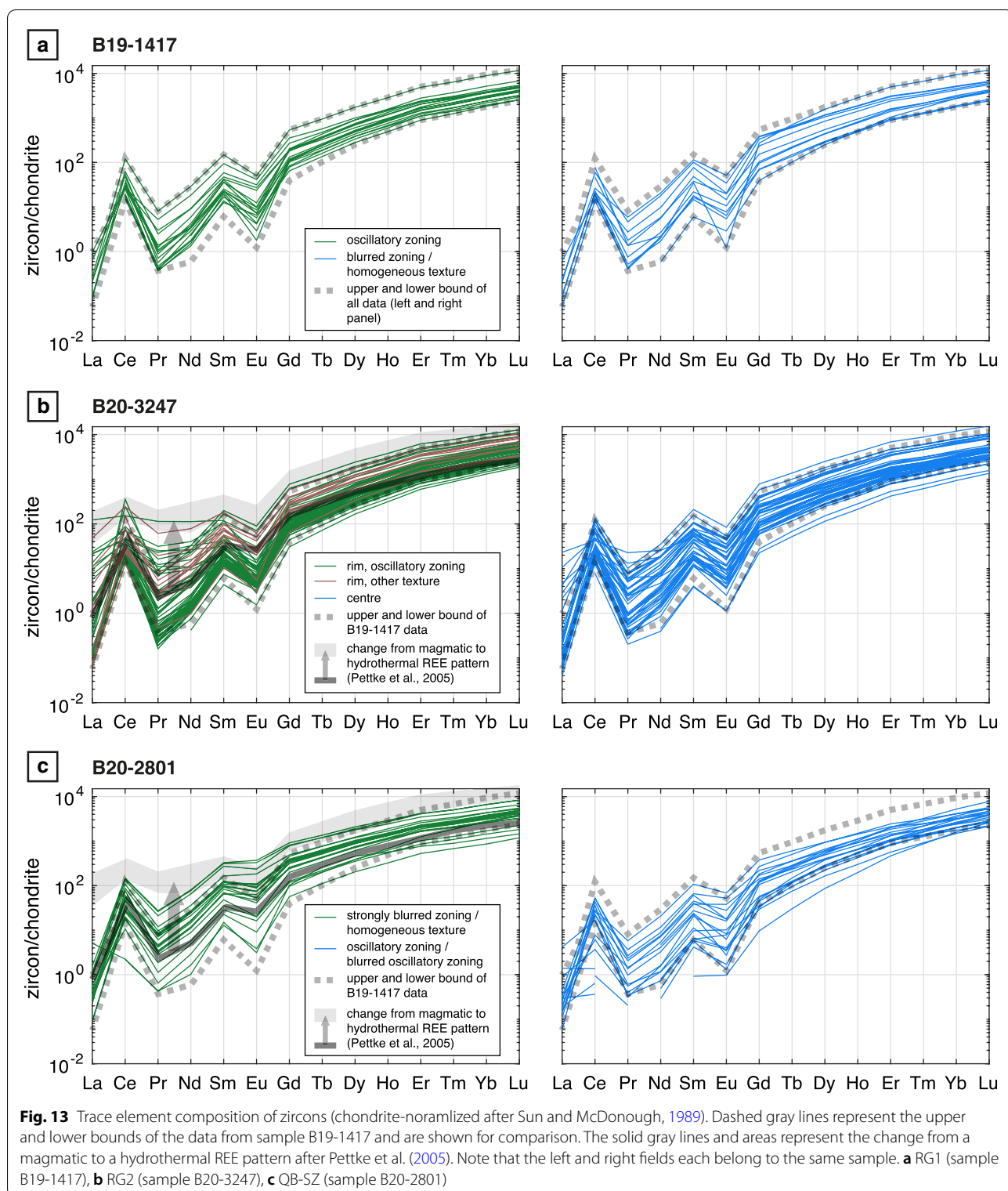
A total of 96 zircons from sample B20-3247 were analysed using CL-imaging. A total of 148 spots were measured by LA-ICP-MS. Of these, 87 measurements were performed in domains with oscillatory zoning (Figs. 15a and b), 33 in domains with blurred texture (Fig. 15c), 27 in almost homogeneous domains (Fig. 15b), and one close to a domain with a ‘spongy texture’. From 88 measurements performed in rims (Figs. 15a and b), 84% were measured



in domains with oscillatory zoning, and from 60 measurements performed in centers (Fig. 15a–c), 78% have a blurred or almost homogeneous texture.

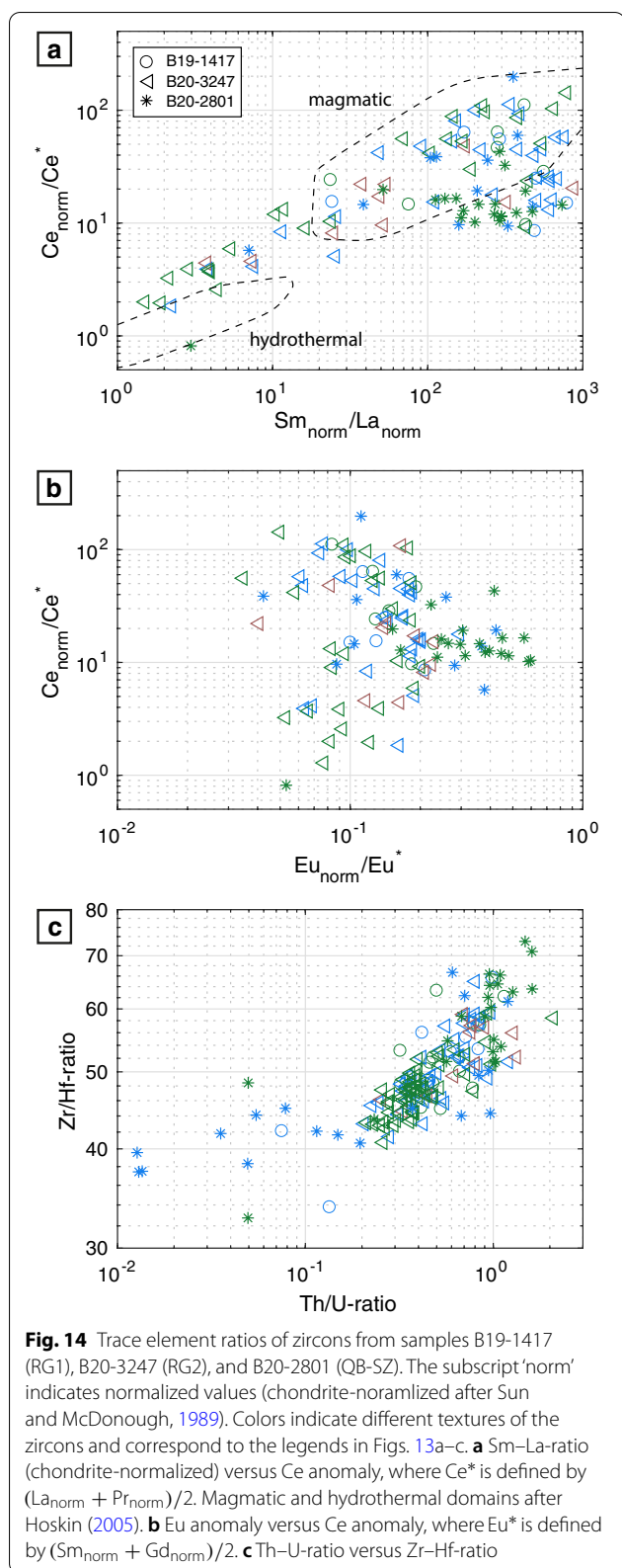
A total of 25 data points were discarded due to discordance or other indications on considerable Pb loss (see Additional file 4), and two data points suggest an inherited core, leaving a total of 121 data points considered for the age determination (Figs. 15d and e). For the determination of the mean age, another outlier was discarded based on a modified version of Chauvenet's

criterion (Vermeesch, 2018) (brightened bar in Fig. 15e). The considered $^{206}\text{Pb}/^{238}\text{U}$ -ages have a range of 280–335 Ma with a distinct peak at ~ 294 Ma and a mean of 295.2 ± 3.6 Ma (Fig. 15e). However, the mean is related to an MSWD value of 10.6, which indicates a scatter in the age distribution that cannot be attributed to measurement uncertainties (see Sect. 4.2.1), and the presented



mean age again does not correspond to a precise geological event (see also discussion in Sect. 5.3). No relation

occurs between age and zircon texture, or between age and LA-ICP-MS spot location (rim or center, Fig. 15e).



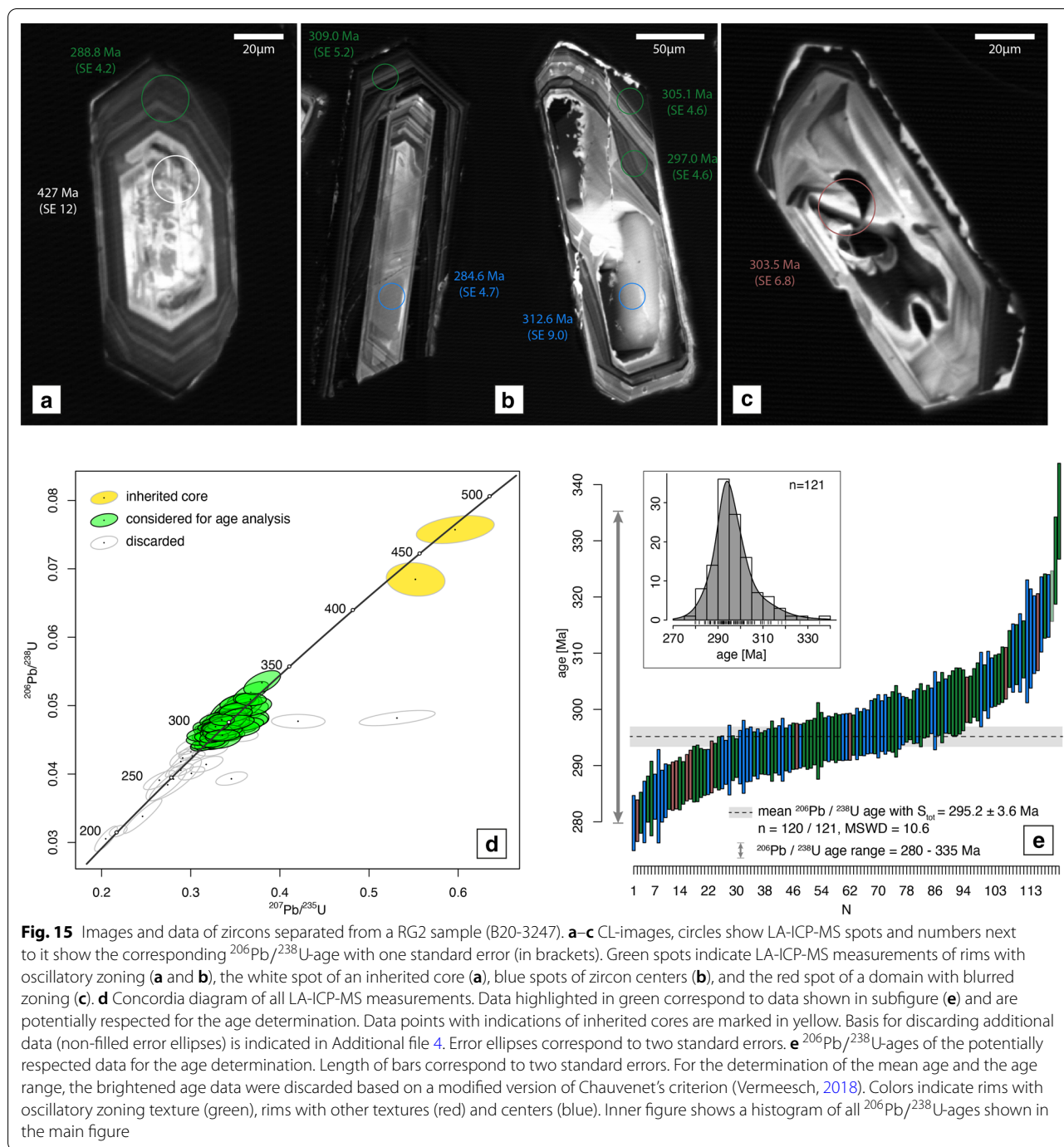
The zircons of sample B20-3247 show a similar REE pattern as the zircons from B19-1417, with generally steep slopes (Fig. 13b), especially in the LREE ($Sm_{norm}/La_{norm} = 0.98$ –1270, average 250, Fig. 14a). However, some zircons have almost flat or negative LREE slopes (low Sm_{norm}/La_{norm} , see Fig. 14a). Similar to sample B19-1417, the zircons of sample B20-3247 exhibit a positive Ce anomaly with an average of 35 and a negative Eu anomaly of 0.13 ± 0.05 (Fig. 14b). However, the Ce anomaly varies strongly (1.3–143), with the low Ce anomalies being related to the low Sm_{norm}/La_{norm} ratios (Fig. 14a). The Th–U-ratios and Zr–Hf-ratios are similar to the zircons of sample B19-1417, with average values of 0.52 ± 0.28 and 49 ± 5 , respectively (Fig. 14c). The trace element composition does not correlate with different types of zircon texture.

4.2.3 Quartz-biotite-rich shear zone (QB-SZ)

A total of 55 zircons from sample B20-2801 were analysed by CL-imaging. A total of 58 spots were measured by LA-ICP-MS. Of these, 22 data points were obtained from grains with oscillatory zoning (Fig. 16a) or grains with blurred oscillatory zoning (Fig. 16b), and 36 from grains with strongly blurred zoning (Fig. 16c) or grains with an almost homogeneous texture (with the exception of a 'ghost texture', Fig. 16d).

Ten data points were discarded due to discordance or other indications on considerable Pb loss (see Additional file 4), and two data points are considerably outside the age range of the other zircons (indicated as 'inherited core'), leaving a total of 46 data points considered for the age analysis (Fig. 16e). The latter data points display a peak between 252 and 303 Ma, mostly defined by zircons with a strongly blurred or almost homogeneous texture, and ages between 325 and 589 Ma without distinct peak(s), mostly corresponding to (\pm blurred) oscillatory zoned zircons (Fig. 16f).

The chondrite-normalized REE pattern of concordant zircons is characterized by steep slopes (Fig. 13c), in particular from La to Sm, with a Sm_{norm}/La_{norm} ratio of 220 ± 170 (Fig. 14a). Furthermore, the zircons exhibit positive Ce anomalies, with an average of 24 (wide range from 0.8 to 198) and negative Eu anomalies of 0.27 ± 0.15 (Fig. 14b). The positive Ce anomaly is more pronounced for zircons with preserved magmatic zoning (5.7–198, average 40) than for zircons with strongly blurred zoning or homogeneous texture (0.8–43, average 16). The same applies to the negative Eu anomalies, with lower Eu_{norm}/Eu^* values for zircons with preserved magmatic zoning (0.04–0.42, average 0.20) than for zircons with strongly blurred zoning or almost homogeneous texture (0.05–0.60, average 0.33). The zircons from the QB-SZ show a similar chondrite-normalized trace

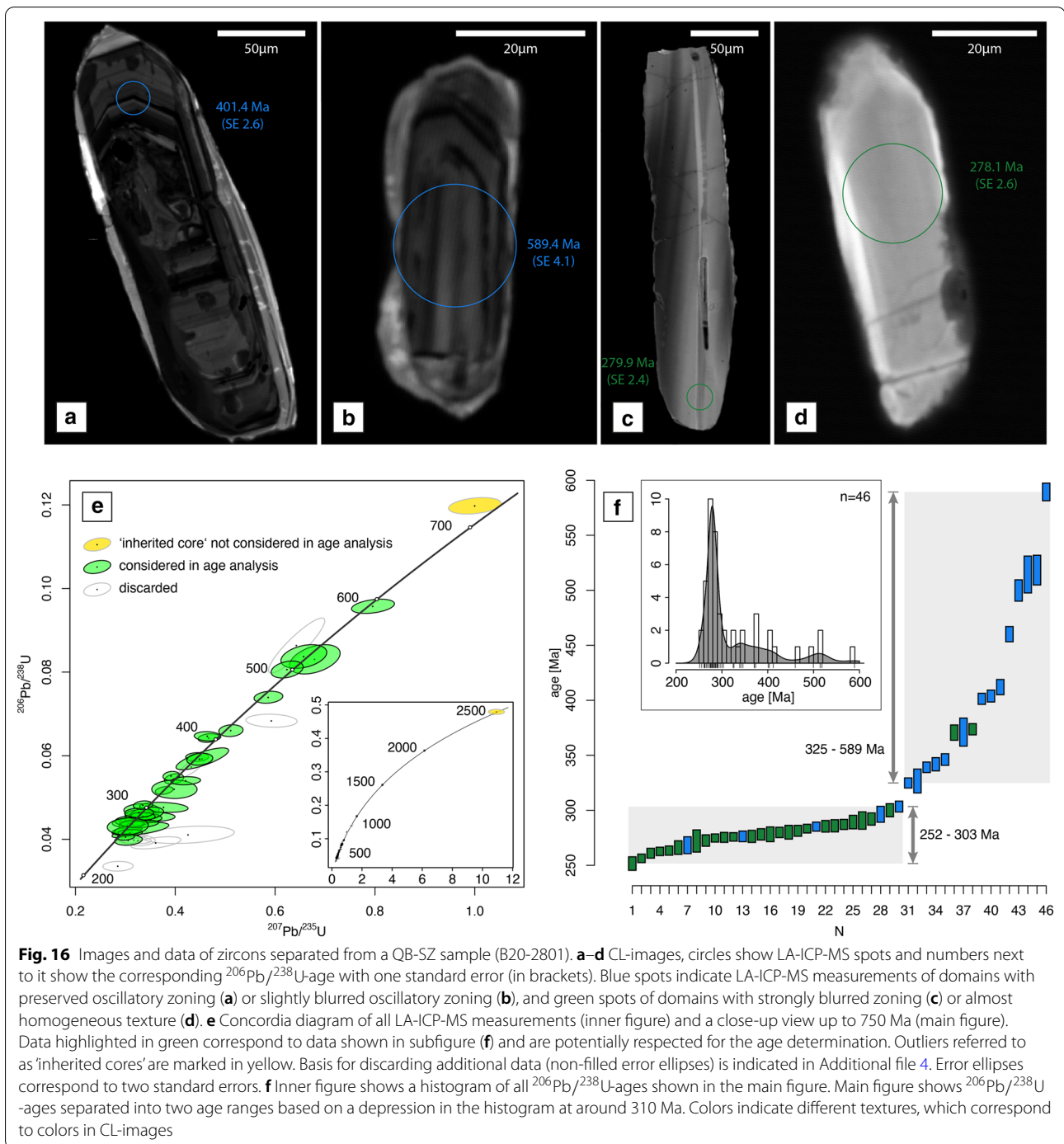


element pattern as the zircons from RG1 (sample B19-1417, Fig. 13c). However, some zircons with strongly blurred zoning or almost homogeneous texture differ from the pattern of sample B19-1417 by generally higher normalized LREE values, less pronounced negative Eu anomalies, and a flatter slope from Sm to Lu (green data in Fig. 13c).

5 Discussion

5.1 Petrology

The petrology along the Bedretto tunnel is described in high spatial resolution in the tunnel section of Schneider (1985) and corresponds well to the petrological observations of the present study. The porphyritic variety of the Rotondo granite (RG2) is not described in studies that were conducted at the surface (e.g. Hafner, 1958;



Steck, 1976). However, in the tunnel section of Schneider (1985), a biotite-rich porphyritic granite with feldspar porphyroclasts has been mapped, although the sharp contact to the equigranular variety of the Rotondo granite (RG1) in the NW and the separation of the two varieties by a QB-SZ in the SE was not reported. The composition of the Rotondo granite in the Bedretto tunnel is

consistent with that reported in other studies (Hafner, 1958; Steck, 1976; Labhart, 2005, Table 1). Garnet within alkali feldspar grains, as well as the lack of indications for metamorphic reactions with garnet growth, indicate a magmatic origin. Magmatic garnet is commonly found in peraluminous granites, which in turn fits with the presence of white mica (Barbarin, 1999).

The macroscopic similarities of the enclave observed at TM 3435 (Fig. 9a) to RG2 indicate that this is a magmatic enclave of RG2 within RG1. This interpretation is further supported by the close proximity between the magmatic enclave and the RG2-RG1 contact (about 4 m). The diffuse character of the contact between magmatic enclave and surrounding granite suggests that both RG1 and RG2 existed contemporaneously under sub-solidus conditions and, hence, both lithologies formed at approximately the same time. In contrast, melanocratic, biotite-rich, and feldspars-poor enclaves have sharp contacts to the granite (Fig. 9b), indicating the incorporation of host rocks. The presence of calcite, the absence of amphiboles, and the abundance of quartz relative to feldspars suggests that these are metasedimentary rocks, i.e. garnet–epidote–calcite bearing paragneisses. Although a foliation is only weakly developed (Fig. 9c), the sharp contact and the mineral paragenesis suggest an interpretation of these enclaves as xenoliths. The mineralogical composition of the xenoliths is in the range of paragneisses of the southern Gottard massif, e.g. of the Prato series or Sorescia gneiss (see summaries of mineralogical contents in Labhart, 2005).

5.2 Deformation of the Rotondo granite

The crosscutting relationship between compositional layering in aplitic dykes and the foliation that affects both aplitic dykes and adjacent granite (Fig. 8) shows that the foliation development is younger than the intrusion of the dyke and clearly indicates that the foliation is not of magmatic origin. The similar characteristics of the two differently oriented sets of foliations (Fig. 4b) indicate a change in the stress field under otherwise more or less constant conditions. The distribution of the foliation orientations is similar to the fracture orientations shown by Gischig et al. (2020) and Jordan (2019), supporting the observation that the biotite accumulations defining the foliation localize fractures.

The occurrence of localized shear zones at contacts between (slightly) different rock types suggests that deformation was localized at rheological contacts and is not restricted to bands of weaker rocks (Mancktelow and Pennacchioni, 2005). The conclusion of Mancktelow and Pennacchioni (2005) is based on the observation of paired shear zones at the border of bleached halos that developed due to fluid–rock interaction along brittle fractures. Although such paired shear zones have not been observed in the Rotondo granite, it is suggested that the concept of strain localization at rheological contacts can be expanded to heterogeneities within granites (Figs. 5d and 10a, e.g. Cobbold, 1977; Pennacchioni and Mancktelow, 2007; Wehrens et al., 2017).

A sample of a granitic shear zone (G-SZ) at TM 1350 shows a similar mineralogical content as the wall rocks (Figs. 10d and e). An increased content of white mica and the presence of calcite could result from metasomatic processes that weakened the rock, localizing the strain (e.g. Kerrich et al., 1980; Goncalves et al., 2012). However, the presence of white mica in the relatively undeformed Rotondo granite (Figs. 7b, c, and e) indicates that the white mica in the G-SZ could also reflect the peraluminous character of the Rotondo granite (Sect. 5.1). In contrast, the presence of calcite is restricted to shear zones, indicating a CO₂-bearing fluid resulting from metamorphic reactions that percolates along the anisotropies defined by these shear zones.

The mineralogy of the quartz-biotite-rich shear zones (QB-SZ) differs distinctly from both the Rotondo granite and the (meta-)lamprophyres in the Gotthard massif: the QB-SZ contain more biotite and quartz and a minor proportion of feldspars compared to the Rotondo granite (Figs. 11d–f), while the (meta-)lamprophyres, unlike the QB-SZ, always contain amphibole (hornblende or actinolite, Oberhänsli, 1986, 1987). In contrast, the mineralogy of the QB-SZ is similar to the xenoliths (Fig. 9c). Therefore, xenoliths in the Rotondo granite should be considered as source rocks of the QB-SZ. This also fits with the sharp contact observed between the QB-SZ and relatively undeformed granite, as well as with the fact that both xenoliths and QB-SZ occur in the Bedretto tunnel mainly between TM 2800 and the NW terminus (TM 5218). The sharp contact of the QB-SZ to the relatively undeformed granite contrasts with strain localization at rheological contacts discussed above in connection with the G-SZ. Instead, the strain appears to be confined within the QB-SZ, indicating that these zones were weaker than the granite (Lützenkirchen, 2002).

5.2.1 Implications based on dynamic recrystallization

Two domains of recrystallized quartz occur in both the relatively undeformed Rotondo granite and G-SZ. The irregular, interlobate grain boundaries in the coarse-grained domains (Figs. 7b–d, 10e and f) indicate dynamic recrystallization of quartz by high-temperature grain boundary migration (GBM). This is supported by the occurrence of pinning structures (Fig. 7c) and so-called ‘left-over grains’ (Figs. 7c, d and 10f), which are typical for GBM (e.g. Jessell, 1987; Stipp et al., 2002; Passchier and Trouw, 2005). According to Stipp et al. (2010), typical grain sizes related to GBM are > 120 μm, which is in agreement with the grain size data of quartz in coarse-grained domains of an RG1, RG2, and G-SZ sample (Additional file 1).

For the occurrence of the finer-grained quartz domains, two interpretations are possible: (1) The

dynamic recrystallization of quartz occurred under different conditions and with a different recrystallization mechanism compared to the dynamic recrystallization of quartz in the coarse-grained domains. This resulted in the fine-grained domains, which appear to be younger since they surround the coarse-grained domains. The dynamic recrystallization mechanism in this case would most probably be subgrain rotation (SGR), which is indicated by slightly elongated grains sub-parallel to the foliation (Figs. 7e and 10g, Nishikawa and Takeshita, 2000). According to Stipp et al. (2010), recrystallization by SGR results typically in grain sizes of approximately 40–120 μm . This would fit with grain sizes in the fine-grained domains determined for the G-SZ but not for the RG1 (Additional file 1). (2) Another interpretation is that the grain size of quartz in the fine-grained domains is controlled by the pinning of grain boundaries by secondary phases (e.g. white mica in Fig. 7e), which commonly occurs in polymineralic domains (Herwegh et al., 2011). This is supported by the fact that secondary phases are more common in the fine-grained than in the coarse-grained domains, and it could also explain why subgrains are almost absent, although SGR seems the most probable dynamic recrystallization mechanism. It should also be noted that in the case of the RG1 sample, the grain size distributions of the coarse- and fine-grained domains overlap within one standard deviation (but not in the case of the G-SZ sample, Additional file 1), supporting the second interpretation.

Nevertheless, dynamic recrystallization of quartz by GBM is preserved in the coarse-grained domains, indicating deformation under high-grade conditions at about 500–700 $^{\circ}\text{C}$ (Stipp et al., 2002; Passchier and Trouw, 2005). However, it must be noted that this temperature estimate is dependent on the presence of water, differential stress, and strain rate (e.g. Hobbs, 1985; Passchier and Trouw, 2005; Stipp et al., 2006). Since dynamic recrystallization of quartz by GBM also occurs in relatively undeformed granite, deformation may have taken place at very low strain rate, and thus deformation at lower temperatures cannot be excluded. Furthermore, calcite in G-SZ indicates the presence of fluid (see above), which may affect the microstructures associated with dynamic recrystallization (Stipp et al., 2006).

Deformation at relatively high temperatures is suggested for the QB-SZ, which kinematically fit the G-SZ, by rigid calcite clasts in ductile deformed quartz veins (Fig. 11c): Mancktelow and Pennacchioni (2010) showed that coarse calcite in wet quartz is stronger than the quartz matrix during amphibolite facies metamorphism at around 550 $^{\circ}\text{C}$. Contradictory are the thick lamellar twins observed in calcite within the QB-SZ material (Fig. 11d), which indicate deformation at temperatures

between 150 and 300 $^{\circ}\text{C}$ (Burkhard, 1993). However, these may have developed at a later stage than the deformation of the quartz veins.

A compilation of Alpine peak temperatures by Bousquet et al. (2012) indicates ~ 475 $^{\circ}\text{C}$ at the NW terminus of the Bedretto tunnel (TM 5218) and ~ 500 $^{\circ}\text{C}$ at the SE boundary of the Rotondo granite (TM 1138). An uncertainty of at least ± 25 $^{\circ}\text{C}$ is suggested due to the general uncertainties of metamorphic temperature estimates and the interpolation of the isobars. The rough temperature estimates discussed above show that deformation in the relatively undeformed Rotondo granite, as well as in localized shear zones (G-SZ and QB-SZ), may have occurred when Alpine peak temperature conditions prevailed. This is in agreement with the findings of Oliot et al. (2010), who related the activity of a steeply NW-dipping shear zone in the Fibbia granite to a temperature of 490 $^{\circ}\text{C}$.

In general, dynamic recrystallization of quartz in the Rotondo granite indicates higher-grade conditions (GBM) than those reported for the Aar massif, where dynamic recrystallization of quartz by SGR at the southeastern boundary of the massif and decreasing grade (bulging, BLG) towards NW was observed (Bambauer et al., 2009). This corresponds to an Alpine metamorphic gradient with increasing temperature from NW to SE (Bousquet et al., 2012).

5.2.2 Kinematics

Both G-SZ and QB-SZ are similarly oriented with a relative upward movement of the northern block (Fig. 3a), which indicates that both types of shear zones were active in a similarly oriented stress field. The orientation of the shear zones (moderately to steeply dipping towards N) is similar to a set of foliations mapped by Schneider (1985) (Fig. 4b). This suggests that the shear zones localized at weak planes defined by the foliation, or that the foliation was formed by slight shear (in a similarly oriented stress field as during shear zone formation).

If it is assumed that the ductile shear zones developed during the Alpine orogenesis, the following considerations show that they do not fit to the 'D2 stage' nor the 'D4 stage' and thus are most probably related to the 'D3 stage' (steepening and partial overturning of the Gotthard massif, Fig. 2c): (1) The kinematics of the shear zones (upward movement of the northern block) do not fit with northward thrusting of the Gotthard massif during 'D2 stage' (Figs. 2a and b). Alpine peak temperature was reached after the Gotthard massif was thrust onto the Aar massif during the 'D2 stage' (Herwegh et al., 2017; Ricchi et al., 2019, Sect. 2.2.2). Hence relating the shear zones to the 'D3 stage' is in agreement with the rough temperature constraints discussed above (Sect. 5.2.1),

which suggest that the shear zones were active at around the time when Alpine metamorphic temperatures were at their peak. (2) Based on crosscutting relationships, Herwegh et al. (2017) showed that NW dipping dextral strike slip faults observed in the southern Aar massif post-date structures of the ‘D3 stage’ (Fig. 2d). These faults have been associated to the ‘D4 stage’ (‘Oberaar’ phase) based on Th–Pb crystallization ages of fissure monazite (Ricchi et al., 2019). In the Rotondo granite, similarly oriented dextral strike-slip faults localized along pre-existing ductile shear zones (Lützenkirchen and Loew, 2011), suggesting that the shear zones pre-date the ‘D4 stage’. Furthermore, this is supported by the fact that the rough temperature estimate for the shear zones (Sect. 5.2.1) is higher than the 200–300 °C estimated by Lützenkirchen and Loew (2011) for the strike-slip faults (further discussed below).

Considering a general N-vergent thrusting regime during the main stages of Alpine orogenesis (Sect. 2.2.2), the kinematics of the ductile shear zones in the Rotondo granite must be related to backthrusting. If one would assume that these shear zones formed earlier and were overturned by Basòdino-Cristallina folding, the shear zones would indicate a normal sense of shearing that does not fit into any of the known Alpine deformation stages. Moreover, the ductile characteristics make it unlikely that they are inherited normal faults related to rifting. Therefore, it is suggested that the backthrusts along the shear zones are a part of the scenario during the ‘D3 stage’ in the Gotthard massif. They developed soon after or during a late stage of the formation of the large-scale synform (Fig. 2c). A kinematic evolution model including backthrusts in the southern Gotthard massif was already proposed by Marquer (1990).

The orientation of brittle faults mapped by Schneider (1985) (> 10 cm wide) is similar to the orientation of the ductile shear zones (Fig. 4b). The agreement is probably even better than it appears in the stereonet, since brittle faults occur more frequently towards the NW terminus of the Bedretto tunnel and the distribution is therefore biased (Fig. 3b). Furthermore, the orientations of ductile shear zones are in the range of NE–SW striking faults mapped by Lützenkirchen and Loew (2011) between TM 3500 and 5218. This supports the interpretation of Lützenkirchen and Loew (2011) that brittle faults have developed along pre-existing ductile shear zones and that these indicate different kinematics than the shear zones, namely dextral strike-slip (Fig. 4b). Based on the fault mineralogy, Lützenkirchen and Loew (2011) estimated that the brittle strike-slip faults were active at temperatures of approximately 200–300 °C. They used these temperatures together with the thermal history of the central Gotthard massif according to Glotzbach et al. (2010) to

estimate that the faults were active between approximately 18 and 14 Ma. This is earlier than the ‘Oberaar’ phase, which took place between ~11.5 and ~7 Ma (Bergemann et al., 2017; Ricchi et al., 2019) or at least after ~14 Ma (Nibourel et al., 2021), although the faults in the Rotondo granite kinematically fit to this phase. Considering the metamorphic peak temperature of about 475–500 °C (Bousquet et al., 2012) at around ~19–18 Ma (Wiederkehr et al., 2009; Berger et al., 2017; Ricchi et al., 2019), it appears that the time estimate of Lützenkirchen and Loew (2011) should be shifted toward younger ages, as suggested for the ‘Oberaar’ phase by Bergemann et al. (2017), Ricchi et al. (2019), and Nibourel et al. (2021).

5.3 Intrusion age of the Rotondo granite

Zircons of two Rotondo granite samples were investigated, one of RG1 (sample B19-1417) and one of RG2 (sample B20-3247). Disturbed oscillatory zoning is more present in zircons from RG1 (Fig. 12d) than in zircons from RG2. However, the zircons with disturbed oscillatory zoning appear to have an insignificant influence on the age determination since their ages are relatively equally distributed over the determined age ranges (Figs. 12f and 15e), and the same applies to measured ‘cores’ in zircons from RG2 (Fig. 15e). Both indicate that a reset of the U–Th–Pb decay system in existing zircons took place at the same time as the crystallization of new zircons or ‘rims’.

Mean age calculations with high MSWD values suggests that geological scattering due to crystallization at different ages or a disturbance of the U–Th–Pb decay system must be considered for both RG1 and RG2, which means that a precise intrusion age cannot be calculated. Consequently, we discuss age ranges instead of mean ages in the following. However, it should be noted that also the age ranges are associated with uncertainties, such as the measurement error of the individual ages within the range and the limitations in detecting data points that are not to be considered (Additional file 4). The $^{206}\text{Pb}/^{238}\text{U}$ -age range of zircons from RG1 (285–319 Ma) lies within the range of zircons from RG2 (280–335 Ma), which leads to the interpretation that both granite varieties are part of the same magmatic episode. This fits with the indications of magma mingling based on a RG2 magmatic enclave within RG1 (Sect. 5.1, Fig. 9a). Furthermore, this interpretation is supported by the kernel density estimates (KDE, Vermeesch, 2012) shown in Fig. 17, with peaks at ~295 Ma (RG1) and ~294 Ma (RG2). The peaks of ~295 Ma and ~294 Ma are consistent with the commonly accepted intrusion age of the Rotondo granite of 294 ± 1.1 Ma (Sergeev et al., 1995). However, the relatively wide age ranges of the presented zircon age data and the fact that the age of Sergeev et al. (1995) is based

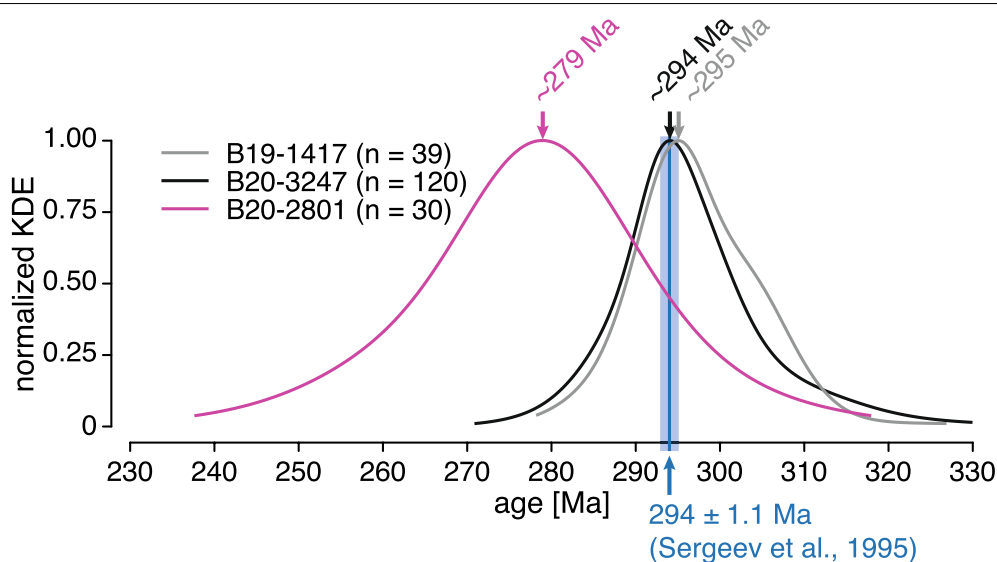


Fig. 17 Kernel density estimates (KDE, Vermeesch, 2012) and approximate peaks of $^{206}\text{Pb}/^{238}\text{U}$ -ages determined for zircons of a RG1 sample (B19-1417), a RG2 sample (B20-3247), and a QB-SZ sample (B20-2801). n -values in brackets correspond to number of considered ages (data used for the mean calculation and age range definition in Figs. 12f and 15e, and data corresponding to the 252–303 Ma age range in Fig. 16f). KDE curves are normalized to a maximum value of one

on a few zircons raise the question of whether their age corresponds to a ‘distinct’ intrusion event or represents a mixed age of a range, as in the data presented in this study.

Both granite samples contain zircons with Th–U-ratios > 0.07, enrichment of HREE over LREE, positive Ce anomalies, and negative Eu anomalies, which points to zircons of magmatic origin (Hoskin and Schaltegger, 2003; Rubatto, 2002). A few zircons from sample B20-3247 (RG2) show less pronounced Ce anomalies and less fractionated LREE (Figs. 13b and 14a), as usually reported from hydrothermal zircons (Pettke et al., 2005; Hoskin, 2005). Similarly, the occurrence of ‘spongy textures’ in zircons from both RG1 and RG2 suggests hydrothermal activity (Corfu et al., 2003). In addition, hydrothermal activity is indicated by data points that were discarded due to discordance or indications on Pb loss (Figs. 12e and 15d, see also Additional file 4). Therefore, the relatively large ranges of discordant ages (34 Myr in RG1 and 55 Myr in RG2) are interpreted to be due to a disturbance of the U–Th–Pb decay system by late- to post-magmatic fluids.

Although an exact intrusion age cannot be demonstrated, the age ranges of RG1 and RG2 show that the Rotondo granite can be attributed to a late- to post-Variscan magmatic episode as commonly proposed in the literature (e.g. Schaltegger, 1994; Sergeev et al., 1995; Labhart, 2005). The Rotondo granite thus joins a series of magmatic bodies in the Central Alps that have intruded

during the same period, such as the nearby Fibbia granite with an intrusion age of 299.4 ± 1.2 Ma (Sergeev et al., 1995), the Central Aar granite s.str. in the Aar massif with an intrusion age of 299 ± 2 Ma (Schaltegger and Corfu, 1992), or the Alpigia complex (Leptontine Alps), of which the pre-metamorphic protolith is attributed to an intrusion at around 292 Ma (Hirsiger et al., 2015). The late-Carboniferous to early-Permian magmatic episode in the basement units of the Central Alps is often interpreted to be related to extension and lithospheric thinning during the latest stages of Variscan orogeny caused by gravitational collapse (Schaltegger, 1997; Schaltegger and Gebauer, 1999; Vanderhaeghe et al., 2020). This is preserved in several areas in Central Europe, such as the Massif Central (e.g. Vanderhaeghe et al., 2020), Vosges (e.g. Soder and Romer, 2018), or Bohemian massif (e.g. Schulmann et al., 2014).

5.4 Source rock of QB-SZ

Zircons of a quartz-biotite-rich shear zone (QB-SZ) located between TM 2800 and TM 2805 (sample B20-2801) were investigated to obtain indications of the parent material of the deformed rocks and constraints on the timing of deformation. Sample B20-2801 contains zircons with preserved oscillatory zoning, of which 14 data points out of 19 have concordant ages between 325 and 589 Ma, and strongly blurred or almost homogeneous zircons, of which 25 data points out of 27 have concordant ages between 252 and 303 Ma (Fig. 16f).

Approximately one third of the concordant data points are older than the upper boundary of the granite age ranges (335 Ma for B20-3247, Sect. 5.3). In contrast, both granite samples contain only rare inherited cores. This leads to the interpretation that the QB-SZ are not sheared lamprophyres that are cogenetic with the host Rotondo granite, as previously thought (e.g. Schneider, 1985; Lützenkirchen, 2002; Lützenkirchen and Loew, 2011). The abundant occurrence of pre-Carboniferous zircons in the QB-SZ rather suggests that the QB-SZ are strongly sheared basement paragneiss xenoliths. Numerous xenoliths within the Rotondo granite have a similar composition as the QB-SZ (Sect. 5.2), which reinforces this interpretation.

In both, zircons with disturbed textures (strongly blurred zoning or almost homogeneous textures) and with preserved oscillatory zoning, the normalized REE pattern is similar to that of RG1 (sample B19-1417, Fig. 13c) and corresponds to a typical magmatic pattern with steep slopes in the LREE, positive Ce anomalies, and negative Eu anomalies (e.g. Rubatto, 2002; Hoskin and Schaltegger, 2003). However, ages ranging from 252 to 303 Ma are mainly defined by zircons with strongly blurred or almost homogeneous texture, and such textures in zircons are usually characteristic for medium- to high-temperature metamorphism or hydrothermal zircons (Corfu et al., 2003). This suggests that the change from magmatically zoned to blurred textures resulted from a metamorphic event or by fluid-zircon interaction, which may have led to a (partial) reset of the U–Th–Pb decay system. Furthermore, the presence of syn-kinematic quartz veins with calcite in the studied QB-SZ (Figs. 11b and c) raises the question whether the zircons with disturbed texture were affected by hydrothermal fluids. A normalized REE pattern that indicates a change from magmatic to hydrothermal zircons is not observed in zircons from the QB-SZ (Fig. 13c). In a Sm–La-ratio versus Ce anomaly diagram after Hoskin (2005), only two data points plot close to the hydrothermal domain, while the others are close to the magmatic domain (Fig. 14a). However, hydrothermal zircons can result in different normalized REE patterns (Pettke et al., 2005). Therefore, a hydrothermal origin or overprint of zircons with strongly blurred zoning or almost homogeneous textures do not appear to be evident from the trace element composition, but cannot be excluded either.

Although the age range from 252 to 303 Ma overlaps with the age ranges of the zircons from the granite samples, the KDE shows a distinct peak around ~279 Ma, which is younger than the peaks of the granite samples (Fig. 17). There are two possible interpretations for the observed zircon age distribution: (1) In some zircons, a reset of the U–Th–Pb decay system occurred after

the emplacement of the Rotondo granite by late- to post-magmatic fluids. Such an explanation would be in agreement with Sergeev and Steiger (1993), who dated ~270 Ma old zircons separated from metasomatic microcline in the Rotondo granite and interpreted them as zircons affected by post-intrusive recrystallization. However, the age data of the Rotondo granite samples show that their data may simply be at the lower end of the age range and cannot be attributed to a distinct event. (2) The partial resetting of the U–Th–Pb decay system in zircons from the QB-SZ is related to the intrusion of the Rotondo granite, the tendency towards younger ages being related to increased Pb loss. Although Pb loss may lead to discordant ages, its detection is limited by the analytical uncertainties of the applied method. A possibility to overcome the issue of Pb loss is to analyse $^{207}\text{Pb}/^{206}\text{Pb}$ -ages, which are not affected by Pb loss. However, this was not feasible since the uncertainties of the $^{207}\text{Pb}/^{206}\text{Pb}$ -ages are too large. Nevertheless, the second interpretation is supported by the large range from 252 to 303 Ma, which shows a potential reset of the U–Th–Pb decay system. However, the question remains why Pb loss was more effective in the zircons from the QB-SZ in comparison to the zircons from the Rotondo granite, which can be possibly attributed to increased hydrothermal activity due to shearing in the QB-SZ. Overall, it remains unclear what the meaning of the age range between 252 and 303 Ma in zircons from the QB-SZ is, and a correlation to shear activity cannot be demonstrated.

6 Conclusions

This paper summarizes the geology and tectonic evolution on a regional (Gotthard massif) and local (Bedretto tunnel) scale and at the same time provides a basis for ongoing and future studies in the Bedretto Underground Laboratory for Geosciences and Geoenergies. New data resulting from field observations, microstructural observations, and zircon investigations provide the following insights into geochronology and ductile deformation in the Rotondo granite:

1. Ductile shear zones observed in the Rotondo granite can be subdivided based on their mineralogy into granitic shear zones (G-SZ) and quartz-biotite-rich shear zones (QB-SZ). Both G-SZ and QB-SZ generally dip moderately to steeply towards north and are generally related to reverse shearing with relative upward movement of the northern block. The shear zones in the Rotondo granite are attributed to back-thrusting during the late exhumation phase of the Gotthard massif (Alpine 'D3 stage').

2. The development of G-SZ occurred preferentially at rheological contacts within the granite. The parent material of the QB-SZ is interpreted as xenoliths (based on U–Pb geochronology, see below). The sharp contact between the QB-SZ and relatively undeformed granite suggests that, where weaker xenoliths were embedded within the stronger Rotondo granite, the strain was confined within the QB-SZ.
3. Although an exact intrusion age cannot be demonstrated based on the presented U–Pb zircon data, the data nevertheless show that the two varieties of Rotondo granite (RG1 and RG2) observed in the Bedretto tunnel are part of the same late- to post-Variscan magmatic episode. This is indicated by the overlapping $^{206}\text{Pb}/^{238}\text{U}$ -age ranges of 285–319 Ma (RG1) and 280–335 Ma (RG2).
4. About 30% of the zircons from a QB-SZ sample are older than the upper boundary of the age range defined by zircons from the granite (> 335 Ma). In contrast, the granite samples only contain a non-significant number of inherited cores older than 335 Ma. This indicates that the parent material of the QB-SZ is not cogenetic with the Rotondo granite, as would be the case for a sheared lamprophyre or sheared granite, but rather that the QB-SZ are sheared xenoliths within the granite. The other ~70% of the zircons define a $^{206}\text{Pb}/^{238}\text{U}$ -age range of 252–303 Ma and show indications of a reset of the U–Th–Pb decay system, possibly caused by the intrusion of the Rotondo granite.

Abbreviations

BLG: Bulging; BULGG: Bedretto Underground Laboratory for Geosciences and Geoenergies; CL: Cathodoluminescence; EGS: Engineered Geothermal Systems; RG1: Equigranular Rotondo granite; RG2: Porphyritic Rotondo granite; GBM: Grain boundary migration; G-SZ: Granitic shear zone(s); HREE: Heavy rare-earth elements; KDE: Kernel density estimates; LA-ICP-MS: Laser Ablation-Inductively Coupled Plasma-Mass Spectrometry; LREE: Light rare-earth elements; MSWD: Mean squared weighted deviation; QB-SZ: Quartz-biotite-rich shear zone(s); REE: Rare-earth elements; SEM: Scanning electron microscope; SGR: Subgrain rotation; TM: Tunnel meter.

Supplementary Information

The online version contains supplementary material available at <https://doi.org/10.1186/s00015-022-00409-w>.

Additional file 1. Quartz grain size data. Figure showing the grain size distribution of quartz measured in a G-SZ, QB-SZ, RG1, and RG2 sample. Information on how the data were acquired can be found in the caption.

Additional file 2. LA-ICP-MS metadata. Table with metadata of the LA-ICP-MS operation.

Additional file 3. CL-images. CL-images of zircons used for the geochronological study. LA-ICP-MS spots and corresponding $^{206}\text{Pb}/^{238}\text{U}$ -ages (with one standard error in brackets) are indicated on the images, except for data discarded for the age determination (see Additional file 4).

Additional file 4. Processed LA-ICP-MS data. Table with processed data resulting from the LA-ICP-MS measurements. The last two columns indicate which data were discarded for age determination and/or REE analysis, respectively, including the rationale for discarding.

Acknowledgements

Fruitful discussions with Neil Mancktelow, Daniela Rubatto, Whitney Behr, and Luiz Grafalha Morales helped to improve the quality of the manuscript. Miguel Cisnero, Maria Giuditta Fellin, Michaël Mintrone, Zoe Braden, Peter Tollan, and Gino Sartori are acknowledged for analytical support. We thank Marian Hertrich and Quinn Wenning for logistical support in the BULGG. We would also like to express our gratitude to Michael Stipp and two anonymous reviewers for critical and constructive comments.

Authors' contributions

MR, AG, and JR designed the study, carried out the field work, collected the samples, and acquired and interpreted the analytical results. MR assembled the figures and wrote the manuscript. CM helped to design the study, coordinate the field work, and interpreting the data. MG helped with LA-ICP-MS analyses, U–Pb data reduction, and interpretation. AG, JR, CM, and MG contributed to the manuscript text and figures through discussion and revision. All authors read and approved the final manuscript.

Funding

Open access funding provided by Swiss Federal Institute of Technology Zurich. No funding was received for conducting this study.

Availability of data and materials

The datasets generated and analysed during this study are included in this published article and its additional information files.

Declarations

Ethics approval and consent to participate

Not applicable.

Consent for publication

Not applicable.

Competing interests

The authors declare that they have no competing interests.

Author details

¹Department of Earth Sciences, Geological Institute, ETH Zürich, Zurich, Switzerland. ²Department of Earth Sciences, Institute of Geochemistry and Petrology, ETH Zürich, Zurich, Switzerland.

Received: 2 July 2021 Accepted: 26 January 2022

Published online: 19 March 2022

References

- Bambauer, H. U., Herwegh, M., & Kroll, H. (2009). Quartz as indicator mineral in the Central Swiss Alps: The quartz recrystallization isograd in the rock series of the northern Aar massif. *Swiss Journal of Geosciences*, 102(2), 345–351. <https://doi.org/10.1007/s00015-009-1319-z>
- Barbarin, B. (1999). A review of the relationships between granitoid types, their origins and their geodynamic environments. *Lithos*, 46, 605–626. [https://doi.org/10.1016/S0024-4937\(98\)00085-1](https://doi.org/10.1016/S0024-4937(98)00085-1)
- Bergemann, C., Gnos, E., Berger, A., Whitehouse, M., Mullis, J., Wehrens, P., Pettke, T., & Janots, E. (2017). Th–Pb ion probe dating of zoned hydrothermal monazite and its implications for repeated shear zone activity:

- An example from the central alps, Switzerland. *Tectonics*, 36(4), 671–689. <https://doi.org/10.1002/2016TC004407>
- Berger, A., Mercolli, I., Herwegh, M., & Gnos, E. (2016). *Geological map of the Aar Massif, Tavetsch and Gotthard nappes, Geological special map No. 129*. Wabern: Federal Office of Topography swisstopo.
- Berger, A., Mercolli, I. P., Herwegh, M., & Gnos, E. (2017). *Explanatory Notes to the Geological map of the Aar massif, Tavetsch and Gotthard nappes, Geological special map No. 129*. Wabern: Federal Office of Topography swisstopo.
- Biino, G. G. (1994). The pre Late Ordovician metamorphic evolution of the Gotthard-Tavetsch massifs (Central Alps): From lawsonite to kyanite eclogites to granulite retrogression. *Schweizerische mineralogische und petrographische Mitteilungen*, 74(1), 87–104. <https://doi.org/10.5169/seals-56333>
- Bousquet, R., Oberhänsli, R., Schmid, S. M., Berger, A., Wiederkehr, M., Robert, C., Möller, A., Rosenberg, C., Zeilinger, G., Molli, G., & Koller, F. (2012). *Metamorphic framework of the Alps (1:1,000,000)*. Paris: Commission for the Geological Map of the World.
- Burkhard, M. (1993). Calcite twins, their geometry, appearance and significance as stress-strain markers and indicators of tectonic regime: A review. *Journal of Structural Geology*, 15, 351–368. [https://doi.org/10.1016/0191-8141\(93\)90132-T](https://doi.org/10.1016/0191-8141(93)90132-T)
- Cardozo, N., & Allmendinger, R. W. (2013). Spherical projections with OSXSteereonet. *Computers & Geosciences*, 51, 193–205. <https://doi.org/10.1016/j.cageo.2012.07.021>
- Cobbold, P. R. (1977). Description and origin of banded deformation structures. II. Rheology and the growth of banded perturbations. *Canadian Journal of Earth Sciences*, 14(11), 2510–2523. <https://doi.org/10.1139/e77-217>
- Corfu, F., Hancher, J. M., Hoskin, P. W. O., & Kinny, P. (2003). Atlas of zircon textures. *Reviews in Mineralogy and Geochemistry*, 53(1), 469–500. <https://doi.org/10.2113/0530469>
- Federal Office of Topography swisstopo. (2011). swissALTI3D multidirectional Hillshade. Retrieved January 8, 2020 from <https://s.geo.admin.ch/86b1e4783b>.
- Federal Office of Topography swisstopo. (2016). Geological overview of Switzerland. Retrieved January 14, 2020 from <https://shop.swisstopo.admin.ch/en/products/accessories/postcards>.
- Gischig, V. S., Giardini, D., Amann, F., Herrlich, M., Krietsch, H., Loew, S., Maurer, H., Villiger, L., Wiemer, S., Bethmann, F., Brixel, B., Doetsch, J., Doonechaly, N. G., Driesner, T., Dutler, N., Evans, K. F., Jalali, M., Jordan, D., Kittilä, A., ... Valley, B. (2020). Hydraulic stimulation and fluid circulation experiments in underground laboratories: Stepping up the scale towards engineered geothermal systems. *Geomechanics for Energy and the Environment*, 24, 100175. <https://doi.org/10.1016/j.gete.2019.100175>
- Glotzbach, C., Reinecker, J., Danisik, M., Rahn, M., Frisch, W., & Spiegel, C. (2010). Thermal history of the central Gotthard and Aar massifs, European Alps: Evidence for steady state, long-term exhumation. *Journal of Geophysical Research*, 115, 111–124. <https://doi.org/10.1029/2009JF001304>
- Goncalves, P., Oliot, E., Marquer, D., & Connolly, J. A. (2012). Role of chemical processes on shear zone formation: An example from the grimsel metagranodiorite (Aar massif, Central Alps). *Journal of Metamorphic Geology*, 30(7), 703–722. <https://doi.org/10.1111/j.1525-1314.2012.00991.x>
- Grujic, D., & Mancktelow, N. S. (1996). Structure of the northern Maggia and Lebendun Nappes, Central Alps, Switzerland. *Eclogae Geologicae Helveticae*, 89(1), 461–504. <https://doi.org/10.5169/seals-167910>
- Guerrot, C., & Steiger, R. H. (1991). Variscan granitoids in the Gotthard-massif, Switzerland: Pb-U single zircon and Sr-Nd data. *Terra Abstracts*, 3(1), 35.
- Hafner, S. (1958). Petrographie des südwestlichen Gotthardmassivs (zwischen St.-Gotthardpass und Nufenenpass). *Schweizerische mineralogische und petrographische Mitteilungen*, 38(2), 255–362. <https://doi.org/10.5169/seals-29611>
- Hafner, S., Günthert, A., Burckhardt, C. E., Steiger, R. H., Hansen, J. W., & Niggli, C. R. (1975). *Geologischer Atlas der Schweiz 1:25000, Val Bedretto, Atlasblatt 68*. Schweizerische Geologische Kommission.
- Herwegh, M., Berger, A., Baumberger, R., Wehrens, P., & Kissling, E. (2017). Large-scale crustal-block-extrusion during late Alpine collision. *Scientific Reports*, 7(1), 1–10. <https://doi.org/10.1038/s41598-017-00440-0>
- Herwegh, M., Linckens, J., Ebert, A., Berger, A., & Brodhag, S. H. (2011). The role of second phases for controlling microstructural evolution in polymineralic rocks: A review. *Journal of Structural Geology*, 33(12), 1728–1750. <https://doi.org/10.1016/j.jsg.2011.08.011>
- Hirsiger, C., Bussy, F., Epard, J.-L., Masson, H., Steck, A., & Ulianov, A. (2015). The Lower Permian Alpigia magmatic complex and its country rock (Upper Maggia Valley, Central Alps): Petrology, geochronology and structural position. In *Abstract Volume 13th Swiss geoscience meeting* (pp. 106–107).
- Hobbs, B. E. (1985). The geological significance of microfabric analysis. In H.-R. Wenk (Ed.), *Preferred orientation in deformed metal and rocks* (pp. 463–484). San Diego: Academic Press. <https://doi.org/10.1016/B978-0-12-744020-0.50027-4>
- Horstwood, M. S. A., Koler, J., Gehrels, G., Jackson, S. E., McLean, N. M., Paton, C., Pearson, N. J., Sircombe, K., Sylvester, P., Vermeesch, P., Bowring, J. F., Condon, D. J., & Schoene, B. (2016). Community-derived standards for LA-ICP-MS U-(Th)-Pb geochronology — Uncertainty propagation, age interpretation and data reporting. *Geostandards and Geoanalytical Research*, 40(3), 311–332. <https://doi.org/10.1111/j.1751-908X.2016.00379.x>
- Hoskin, P. W. (2005). Trace-element composition of hydrothermal zircon and the alteration of Hadean zircon from the Jack Hills, Australia. *Geochimica et Cosmochimica Acta*, 69(3), 637–648. <https://doi.org/10.1016/j.gca.2004.07.006>
- Hoskin, P. W. O., & Schaltegger, U. (2003). The composition of zircon and igneous and metamorphic petrogenesis. *Reviews in Mineralogy and Geochemistry*, 53(1), 27–62. <https://doi.org/10.2113/0530027>
- Huber, H. M. (1943). Physiographie und Genesis der Gesteine im südöstlichen Gotthardmassiv. *Schweizerische mineralogische und petrographische Mitteilungen*, 23(1), 72–260. <https://doi.org/10.5169/seals-20057>
- Jackson, S. E., Pearson, N. J., Griffin, W. L., & Belousova, E. A. (2004). The application of laser ablation-inductively coupled plasma-mass spectrometry to in situ U–Pb zircon geochronology. *Chemical Geology*, 211(1–2), 47–69. <https://doi.org/10.1016/j.chemgeo.2004.06.017>
- Jessell, M. W. (1987). Grain-boundary migration microstructures in a naturally deformed quartzite. *Journal of Structural Geology*, 9(8), 1007–1014. [https://doi.org/10.1016/0191-8141\(87\)90008-3](https://doi.org/10.1016/0191-8141(87)90008-3)
- Jordan, D. (2019). *Geological characterization of the Bedretto Underground Laboratory for Geoenergies* (M.Sc thesis). ETH Zürich. <https://doi.org/10.3929/ethz-b-000379305>
- Kamb, W. B. (1959). Ice petrofabric observations from Blue Glacier, Washington, in relation to theory and experiment. *Journal of Geophysical Research*, 64(11), 1896–1977. <https://doi.org/10.1029/JZ064i011p01891>
- Keller, F., & Schneider, T. R. (1982). Geologie und Geotechnik. *Schweizer Ingenieur und Architekt*, 100(24), 512–520. <https://doi.org/10.5169/seals-74820>
- Keller, F., Wanner, H., & Schneider, T. R. (1987). *Geologischer Schlussbericht Gotthard-Strassentunnel: Zusammenfassung*. Bern: Kümmerli und Frey.
- Kennedy, A. K., Wotzlaw, J. F., Schaltegger, U., Crowley, J. L., & Schmitz, M. (2014). Eocene zircon reference material for microanalysis of U-Th-Pb isotopes and trace elements. *Canadian Mineralogist*, 52(3), 409–421. <https://doi.org/10.3749/canmin.52.3.409>
- Kerrich, R., Allison, I., Barnett, R. L., Moss, S., & Starkey, J. (1980). Microstructural and chemical transformations accompanying deformation of granite in a shear zone at Miéville, Switzerland; with implications for stress corrosion cracking and superplastic flow. *Contributions to Mineralogy and Petrology*, 73, 221–242. <https://doi.org/10.1007/BF00381442>
- Kissling, E., Labhart, T. P., & Rybach, L. (1978). Radiometrische Untersuchungen am Rotondogranit. *Schweizerische mineralogische und petrographische Mitteilungen*, 58(3), 357–388. <https://doi.org/10.5169/seals-45208>
- Labhart, T. P. (2005). *Erläuterungen zum Geologischen Atlas der Schweiz 1:25000, Val Bedretto, Atlasblatt 68*. Bern-Iltigen: Bundesamt für Wasser und Geologie.
- Lützenkirchen, V., & Loew, S. (2011). Late Alpine brittle faulting in the Rotondo granite (Switzerland): Deformation mechanisms and fault evolution. *Swiss Journal of Geosciences*, 104(1), 31–54. <https://doi.org/10.1007/s00015-010-0050-0>
- Lützenkirchen, V. H. (2002). *Structural geology and hydrogeology of brittle fault zones in the Central and Eastern Gotthard Massif, Switzerland* (Ph.D. Thesis). ETH Zürich. <https://doi.org/10.3929/ethz-a-004522949>
- Mancktelow, N. S., & Pennacchioni, G. (2005). The control of precursor brittle fracture and fluid-rock interaction on the development of single and paired ductile shear zones. *Journal of Structural Geology*, 27(4), 645–661. <https://doi.org/10.1016/j.jsg.2004.12.001>
- Mancktelow, N. S., & Pennacchioni, G. (2010). Why calcite can be stronger than quartz. *Journal of Geophysical Research: Solid Earth*, 115(B01402), 100175. <https://doi.org/10.1029/2009JB006526>
- Marquer, D. (1990). Structure et déformation alpine dans les granites hercyniens du massif du Gothard (Alpes centrales suisses). *Eclogae Geologicae Helveticae*, 83(1), 77–97. <https://doi.org/10.5169/seals-166578>

- Masset, O., & Loew, S. (2010). Hydraulic conductivity distribution in crystalline rocks, derived from inflows to tunnels and galleries in the Central Alps, Switzerland. *Hydrogeology Journal*, 18(4), 863–891. <https://doi.org/10.1007/s10040-009-0569-1>
- Maxelon, M., & Mancktelow, N. S. (2005). Three-dimensional geometry and tectonostratigraphy of the Pennine zone, Central Alps, Switzerland and Northern Italy. *Earth-Science Reviews*, 71(3–4), 171–227. <https://doi.org/10.1016/j.earscirev.2005.01.003>
- Mercolli, I., Biino, G. G., & Abrecht, J. (1994). The lithostratigraphy of the pre-Mesozoic basement of the Gotthard massif: A review. *Schweizerische mineralogische und petrographische Mitteilungen*, 74(1), 29–40. <https://doi.org/10.5169/seals-56329>
- Milnes, A. G. (1974). Structure of the Pennine Zone (Central Alps): A new working hypothesis. *Geological Society of America Bulletin*, 85(11), 1727–1732. [https://doi.org/10.1130/0016-7606\(1974\)85%3C1727:SOTPZC%3E2.0.CO;2](https://doi.org/10.1130/0016-7606(1974)85%3C1727:SOTPZC%3E2.0.CO;2)
- Nibourel, L., Berger, A., Egli, D., Heuberger, S., & Herwegh, M. (2021). Structural and thermal evolution of the eastern Aar Massif: Insights from structural field work and Raman thermometry. *Swiss Journal of Geosciences*, 114(1), 1–43. <https://doi.org/10.1186/s00015-020-00381-3>
- Nishikawa, O., & Takeshita, T. (2000). Progressive lattice misorientation and microstructural development in quartz veins deformed under subgreenschist conditions. *Journal of Structural Geology*, 22(2), 259–276. [https://doi.org/10.1016/S0191-8141\(99\)00147-9](https://doi.org/10.1016/S0191-8141(99)00147-9)
- Norman, M., Pearson, N. J., Sharma, A., & Griffin, W. (1996). Quantitative analysis of trace elements in geological materials by laser ablation ICPMS: Instrumental operating conditions and calibration values of NIST glasses. *Geostandards Newsletter*, 20(2), 247–261. <https://doi.org/10.1111/j.1751-908X.1996.tb00186.x>
- Nunes, P. D., & Steiger, R. H. (1974). A U–Pb zircon, and Rb–Sr and U–Th–Pb whole-rock study of a polymetamorphic terrane in the central Alps, Switzerland. *Contributions to Mineralogy and Petrology*, 47(4), 255–280. <https://doi.org/10.1007/BF00390150>
- Oberhänsli, R. (1986). Geochemistry of meta-lamprophyres from the Central Swiss Alps. *Schweizerische Mineralogische und Petrographische Mitteilungen*, 66(3), 315–342. <https://doi.org/10.5169/seals-50898>
- Oberhänsli, R. (1987). Mineralogy and Alpine metamorphism of meta-lamprophyres from the Central Swiss Alps. *Schweizerische Mineralogische und Petrographische Mitteilungen*, 67(3), 321–338. <https://doi.org/10.5169/seals-51608>
- Oberli, F., Meier, M., & Biino, G. G. (1994). Time constraints on the pre-Variscan magmatic/metamorphic evolution of the Gotthard and Tavetsch units derived from single-zircon U–Pb results. *Schweizerische mineralogische und petrographische Mitteilungen*, 74(3), 483–488. <https://doi.org/10.5169/seals-56363>
- Oliot, E., Goncalves, P., & Marquer, D. (2010). Role of plagioclase and reaction softening in a metagranite shear zone at mid-crustal conditions (Gotthard Massif, Swiss Central Alps). *Journal of Metamorphic Geology*, 28(8), 849–871. <https://doi.org/10.1111/j.1525-1314.2010.00897.x>
- Passchier, C. W., & Trouw, R. A. (2005). *Microtectonics* (2nd ed.). Berlin: Springer. <https://doi.org/10.1007/3-540-29359-0>
- Paton, C., Hellstrom, J., Paul, B., Woodhead, J., & Hergt, J. (2011). Iolite: Freeware for the visualisation and processing of mass spectrometric data. *Journal of Analytical Atomic Spectrometry*, 26(12), 2508–2518. <https://doi.org/10.1039/c1ja10172b>
- Pennacchioni, G., & Mancktelow, N. S. (2007). Nucleation and initial growth of a shear zone network within compositionally and structurally heterogeneous granitoids under amphibolite facies conditions. *Journal of Structural Geology*, 29(11), 1757–1780. <https://doi.org/10.1016/j.jsg.2007.06.002>
- Pettke, T., Audétat, A., Schaltegger, U., & Heinrich, C. A. (2005). Magmatic-to-hydrothermal crystallization in the W–Sn mineralized Mole Granite (NSW, Australia). Part II: Evolving zircon and thorite trace element chemistry. *Chemical Geology*, 220(3–4), 191–213. <https://doi.org/10.1016/j.chemgeo.2005.02.017>
- Pettke, T., & Klaper, E. M. (1992). Zur Petrographie und Deformationsgeschichte des südöstlichen Gotthardmassivs. *Schweizerische mineralogische und petrographische Mitteilungen*, 72(2), 197–211. <https://doi.org/10.5169/seals-54907>
- Pfiffner, O. A. (2010). *Geologie der Alpen* (2nd ed.). Stuttgart: UTB.
- Pfiffner, O. A., Schlunegger, F., & Buitter, S. J. (2002). The Swiss Alps and their peripheral foreland basin: Stratigraphic response to deep crustal processes. *Tectonics*, 21(2), 1–15. <https://doi.org/10.1029/2000tc900039>
- Ricchi, E., Bergemann, C. A., Gnos, E., Berger, A., Rubatto, D., & Whitehouse, M. J. (2019). Constraining deformation phases in the Aar Massif and the Gotthard Nappe (Switzerland) using Th–Pb crystallization ages of fissure monazite–(Ce). *Lithos*, 342–343, 223–238. <https://doi.org/10.1016/j.lithos.2019.04.014>
- Rubatto, D. (2002). Zircon trace element geochemistry: Partitioning with garnet and the link between U–Pb ages and metamorphism. *Chemical Geology*, 184, 123–138. [https://doi.org/10.1016/S0009-2541\(01\)00355-2](https://doi.org/10.1016/S0009-2541(01)00355-2)
- Schaltegger, U. (1994). Unravelling the pre-Mesozoic history of Aar and Gotthard massifs (Central Alps) by isotopic dating: A review. *Schweizerische mineralogische und petrographische Mitteilungen*, 74(1), 41–51. <https://doi.org/10.5169/seals-56330>
- Schaltegger, U. (1997). Magma pulses in the Central Variscan Belt: Episodic melt generation and emplacement during lithospheric thinning. *Terra Nova*, 9(5–6), 242–245. <https://doi.org/10.1111/j.1365-3121.1997.tb00021.x>
- Schaltegger, U., & Corfu, F. (1992). The age and source of late Hercynian magmatism in the central Alps: Evidence from precise U–Pb ages and initial Hf isotopes. *Contributions to Mineralogy and Petrology*, 111, 329–344. <https://doi.org/10.1007/BF00311195>
- Schaltegger, U., & Gebauer, D. (1999). Pre-Alpine geochronology of the Central, Western and Southern Alps. *Schweizerische mineralogische und petrographische Mitteilungen*, 79(1), 79–87. <https://doi.org/10.5169/seals-60199>
- Schmid, S., Pfiffner, O. A., & Schreuer, G. (1997). Rifting and collision in the Pennine zone of eastern Switzerland. *Deep structure of the Swiss Alps: Results of NRP 20* (pp. 160–185). Basel: Birkhäuser.
- Schneider, T. (1985). *Basistunnel Furka - Geologische Aufnahme des Fensters Bedretto*. Technical report, Furka-Oberalp-Bahn AG, Brig.
- Schulmann, K., Lexa, O., Janoušek, V., Lardeaux, J. M., & Edel, J. B. (2014). Anatomy of a diffuse cryptic suture zone: An example from the Bohemian Massif, European Variscides. *Geology*, 42(4), 275–278. <https://doi.org/10.1130/G35290.1>
- Sergeev, S. A., Meier, M., & Steiger, R. H. (1995). Improving the resolution of single-grain U/Pb dating by use of zircon extracted from feldspar: Application to the Variscan magmatic cycle in the central Alps. *Earth and Planetary Science Letters*, 134(1–2), 37–51. [https://doi.org/10.1016/0012-821X\(95\)00105-L](https://doi.org/10.1016/0012-821X(95)00105-L)
- Sergeev, S. A., & Steiger, R. H. (1993). High-precision U–Pb single zircon dating of Variscan and Caledonian magmatic cycles in the Gotthard Massif, Central Swiss Alps. *Terra Abstracts*, 5, 394–395.
- Sláma, J., Košler, J., Condon, D. J., Crowley, J. L., Gerdes, A., Hanchar, J. M., Horstwood, M. S., Morris, G. A., Nasdala, L., Norberg, N., Schaltegger, U., Schoene, B., Tubrett, M. N., & Whitehouse, M. J. (2008). Plešovice zircon — A new natural reference material for U–Pb and Hf isotopic microanalysis. *Chemical Geology*, 249(1–2), 1–35. <https://doi.org/10.1016/j.chemgeo.2007.11.005>
- Soder, C. G., & Romer, R. L. (2018). Post-collisional potassic-ultrapotassic magmatism of the variscan orogen: Implications for mantle metasomatism during continental subduction. *Journal of Petrology*, 59(6), 1007–1034. <https://doi.org/10.1093/ptrology/egy053>
- Steck, A. (1976). Albit-Oligoklas-Mineralgesellschaften der Peristeritlücke aus alpinmetamorphen Granitgneisen des Gotthardmassivs. *Schweizerische mineralogische und petrographische Mitteilungen*, 56(2), 269–292. <https://doi.org/10.5169/seals-43687>
- Steck, A., Eparid, J. L., & Masson, H. (2019). The Maggia nappe: An extruding sheath fold basement nappe in the Lepontine gneiss dome of the Central Alps. *International Journal of Earth Sciences*, 108(8), 2429–2442. <https://doi.org/10.1007/s00531-019-01771-1>
- Steiger, R. H. (1962). Petrographie und Geologie des südlichen Gotthardmassivs zwischen St. Gotthard- und Lukmanierpass. *Schweizerische mineralogische und petrographische Mitteilungen*, 42(2), 381–577. <https://doi.org/10.3929/ethz-a-000090198>
- Stipp, M., Stünitz, H., Heilbronner, R., & Schmid, S. M. (2002). The eastern Tonalite fault zone: A 'natural laboratory' for crystal plastic deformation of quartz over a temperature range from 250 to 700 °C. *Journal of Structural Geology*, 24(12), 1861–1884. [https://doi.org/10.1016/S0191-8141\(02\)00035-4](https://doi.org/10.1016/S0191-8141(02)00035-4)
- Stipp, M., Tullis, J., & Behrens, H. (2006). Effect of water on the dislocation creep microstructure and flow stress of quartz and implications for the recrystallized grain size piezometer. *Journal of Geophysical Research: Solid Earth*, 111(4), B04201. <https://doi.org/10.1029/2005JB003852>

- Stipp, M., Tullis, J., Scherwath, M., & Behrmann, J. (2010). A new perspective on paleo-piezometry: Dynamically recrystallized grain size distributions indicate mechanism changes. *Geology*, 38, 759–762. <https://doi.org/10.1130/G31162.1>
- Sun, S. S., & McDonough, W. F. (1989). Chemical and isotopic systematics of oceanic basalts: Implications for mantle composition and processes. *Geological Society Special Publication*, 42(1), 313–345. <https://doi.org/10.1144/GSL.SP.1989.042.01.19>
- Vanderhaeghe, O., Laurent, O., Gardien, V., Moyen, J. F., Gébelin, A., Chelle-Michou, C., Couzinié, S., Villaros, A., & Bellanger, M. (2020). Flow of partially molten crust controlling construction, growth and collapse of the Variscan orogenic belt: The geologic record of the French Massif Central. *BSGF - Earth Sciences Bulletin*, 191, 25. <https://doi.org/10.1051/bsgf/2020013>
- Vermeesch, P. (2012). On the visualisation of detrital age distributions. *Chemical Geology*, 312–313, 190–194. <https://doi.org/10.1016/j.chemgeo.2012.04.021>
- Vermeesch, P. (2018). IsoplotR: A free and open toolbox for geochronology. *Geoscience Frontiers*, 9(5), 1479–1493. <https://doi.org/10.1016/j.gsf.2018.04.001>
- Von Quadt, A., Wotzlaw, J. F., Buret, Y., Large, S. J., Peytcheva, I., & Trinquier, A. (2016). High-precision zircon U/Pb geochronology by ID-TIMS using new 10^{13} ohm resistors. *Journal of Analytical Atomic Spectrometry*, 31(3), 658–665. <https://doi.org/10.1039/c5ja00457h>
- Wehrens, P., Baumberger, R., Berger, A., & Herwegh, M. (2017). How is strain localized in a meta-granitoid, mid-crustal basement section? Spatial distribution of deformation in the central Aar massif (Switzerland). *Journal of Structural Geology*, 94, 47–67. <https://doi.org/10.1016/j.jsg.2016.11.004>
- Wetherill, G. W. (1956). Discordant uranium-lead ages. *Transactions American Geophysical Union*, 37(3), 320–326. <https://doi.org/10.1029/TR037i003p00320>
- Whitney, D. L., & Evans, B. W. (2010). Abbreviations for names of rock-forming minerals. *American Mineralogist*, 95(1), 185–187. <https://doi.org/10.2138/am.2010.3371>
- Wiedenbeck, M., Allé, P., Corfu, F., Griffin, W., Meier, M., Oberli, F., Von Quadt, A., Roddick, J. C., & Spiegel, W. (1995). Three natural zircon standards for U-Th-Pb, Lu-Hf, trace element and REE analyses. *Geostandards Newsletter*, 19, 1–23. <https://doi.org/10.1111/j.1751-908X.1995.tb00147.x>
- Wiederkehr, M., Sudo, M., Bousquet, R., Berger, A., & Schmid, S. M. (2009). Alpine orogenic evolution from subduction to collisional thermal overprint: The $^{40}\text{Ar}/^{39}\text{Ar}$ age constraints from the Valaisan Ocean, central Alps. *Tectonics*, 28(6), 1–28. <https://doi.org/10.1029/2009TC002496>
- Wyss, R. (1986). Die Urseren-Zone - Lithostratigraphie und Tektonik. *Ecologae Geologicae Helveticae*, 79(3), 731–767. <https://doi.org/10.5169/seals-165849>

Publisher's Note

Springer Nature remains neutral with regard to jurisdictional claims in published maps and institutional affiliations.

Submit your manuscript to a SpringerOpen[®] journal and benefit from:

- Convenient online submission
- Rigorous peer review
- Open access: articles freely available online
- High visibility within the field
- Retaining the copyright to your article

Submit your next manuscript at ► [springeropen.com](https://www.springeropen.com)
